September 30, 2025

Independent evolution of holocentric centromeres in an early branching apicomplexan parasite

Running title: Holocentric centromeres in *Cryptosporidium*

Abigail Kimball[1#], Wanyi Huang[1#], Rui Xu[1,a], Melanie Key[1], Lisa Funkhouser-Jones[1,b], and L. David Sibley[1*]

[#] Contributed equally

Department of Molecular Microbiology, Washington University School of Medicine, St. Louis, MO 63110, USA

Present addresses:

[a] State Key Laboratory for Animal Disease Control and Prevention, South China Agricultural University, Guangzhou 510642, China

[b] Department of Microbial Pathogenesis & Immunology, Naresh K. Vashisht School of Medicine, Texas A&M University, Bryan, TX 77807, USA

*Address correspondence to Dr. L. David Sibley, Department of Molecular Microbiology, Washington University School of Medicine, 660 S. Euclid, CB 8230 St. Louis MO 63110. E-mail address: sibley@wustl.edu

Keywords: apicomplexan, mitosis, centromeres, holocentric, *Cryptosporidium*

ABSTRACT

Following host cell invasion by sporozoites, *Cryptosporidium parvum* (*C. parvum*) amplifies rapidly through three rounds of nuclear division prior to undergoing cytokinesis to form infectious merozoites. However, chromosome organization and segregation during nuclear division remain unstudied. Here, we visualized H3-histones, including the centromeric histone H3 (CENH3), telomeres, centrosomes, microtubules, and nuclear pores during mitosis. Nuclear division was accompanied by centriole duplication and elongated microtubules that spanned dividing nuclei. Surprisingly, *C. parvum* centromeres showed diffuse staining throughout nuclear division, and telomeres overlapped with centromeres at the apical nuclear end. Analysis of centromeres based on CENH3 binding and DNA sequencing revealed ~350 distinct binding sites scattered across all eight chromosomes, typified by GA rich repeat sequences. The unique holocentric chromosome structure of *C. parvum* is unlike the single regional centromeres found in related apicomplexans, suggesting it arose independently from other known examples in plants, insects and worms.

INTRODUCTION

Cryptosporidium parvum (C. parvum), an obligate intracellular parasite, remains a serious global health and agricultural threat [1-4]. Transmission occurs through the ingestion of infectious oocysts and causes severe diarrheal illness in infants, young animals, and immunocompromised adults [5-7]. Once ingested, sporozoites exit the oocyst, invade host cells, and undergo three rounds of mitotic division within a single shared cytoplasm (the process of merogony), followed by cytokinesis to produce eight identical merozoites. Newly formed merozoites are released into the lumen, where they invade new host cells, and repeat the

47 invasion-egress cycle three times before transitioning to the sexual phase of the life cycle [8, 9].
48 Despite its significance as a global health problem, and the novelty of apicomplexan cellular
49 division processes, *C. parvum* mitosis remains largely uncharacterized, with our current
50 understanding limited to basic microscopy studies [8, 10-15].

51 To divide rapidly, apicomplexans have evolved mechanisms to streamline mitotic division.
52 Firstly, apicomplexans maintain their chromosomes in an uncondensed state, eliminating the
53 time-consuming steps of chromatin condensation and relaxation and allowing transcription to
54 resume quickly after division [16, 17]. This adaptation necessitates strict nuclear organization
55 during mitosis, where centromeres are typically maintained on the apical end of the nucleus
56 attached to the centrosome and telomeres persistently cluster at the basal end of the nuclear
57 periphery [18-20]. Additionally, apicomplexans maintain their nuclear envelope throughout
58 mitosis, minimizing the energy and time required for breakdown and reformation [17, 21]. A
59 consequence of this closed mitosis is restricted access of spindle fibers to chromosomes,
60 necessitating alternative segregation mechanisms. Rather than centrosomes orchestrating
61 microtubule organization from the cytoplasm, apicomplexan centrosome-like structures (spindle
62 pole bodies, microtubule-organizing centers) are embedded within the nuclear envelope and
63 serve as spindle assembly hubs that elongate the microtubules so they can attach to the
64 centromeres and ultimately coordinate chromosome movement during division [22-29]. Nuclear
65 pores are essential for nucleocytoplasmic transport through the intact envelope and directly
66 support the process of spindle assembly [30, 31]. Electron microscopy studies suggest that *C.*
67 *parvum* undergoes schizogony, with multiple rounds of nuclear replication preceding a
68 cytoplasmic division, followed by the egress of daughter parasites from the host cell. However, it

69 remains unclear whether *C. parvum* replicates its nuclei asynchronously, like *Plasmodium*, or
70 follows a more synchronized division like *Toxoplasma* [17, 32].
71 During mitosis and meiosis, centromeres function to orchestrate chromosome segregation
72 by serving as sites for microtubule anchoring to assure faithful separation at metaphase [33].
73 Centromeres have variable architecture in different organisms consisting of point centromeres
74 (small 250 bp single site per chromosome) in yeast [34], regional centromeres (gene poor islands
75 of heterochromatin ranging from several to hundreds of kb) in *T. gondii* and *P. falciparum* [26,
76 27, 35], and holocentric chromosomes (multiple centromere sites along the chromosome) found
77 in multiple species of plants, insects and worms [36-38]. Although centromere function is
78 essential and highly conserved across eukaryotes, centromeric DNA sequences and size are
79 subject to rapid evolution [39-41]. Variation in centromere architecture affects nuclear
80 organization, karyotype changes, and ultimately drives speciation [42, 43].
81 The nuclear structures, chromosome features, and mitotic mechanisms, including the role of
82 centromeres, have not been examined previously in *C. parvum*. Here, we delineate the
83 fundamental biology of *C. parvum* mitosis, revealing significant deviations from previously
84 assumed mechanisms. Using high-resolution imaging we examined nuclear division during the
85 first round of merogony, leveraging multiple transgenic parasite strains and mitosis-specific
86 antibodies. Additionally, we used Cleavage Under Targets and Nuclease Release (CUT&RUN)
87 [44] to identify the location of the centromeres based on CENH3 and patterns of centromere-
88 associated histone modifications in *C. parvum* and the related parasite *Toxoplasma gondii* (*T.*
89 *gondii*). In contrast to the monocentric centromeric structure of *T. gondii*, we found that *C.*
90 *parvum* has a holocentric chromosome structure with CENH3 binding sites scattered across
91 multiple small regions on all 8 chromosomes, resulting in diffuse CENH3 centromere staining

92 throughout mitosis. Overall, these results suggest that *C. parvum* employs a divergent mitotic
93 mechanism compared to other well-studied apicomplexans and has independently evolved
94 holocentric centromeres.
95
96 **RESULTS**
97 ***Characterization of centromeric histone H3 (CENH3) and histone H3 candidates in C.***
98 ***parvum***
99 The genome annotation of *C. parvum* contains two genes encoding Histone H3 *cgd3_2540* and
100 *cgd4_3220* (referred to here as H3.1 and H3.2, respectively) and a third gene *cgd4_2030*
101 annotated as a centromere-specific Histone H3 variant (CENH3). To validate these annotations,
102 we performed multiple BLASTP analyses using the protein products of each of these three *C.*
103 *parvum* genes to identify top hits in the following groups: 1) Apicomplexa (excluding all
104 *Cryptosporidium* species), 2) all eukaryotic organisms (excluding all Apicomplexa), 3) *Homo*
105 *sapiens*, and 4) *Saccharomyces cerevisiae.* Collectively, these analyses provide strong support
106 for cgd4_2030 as the CENH3 ortholog in *C. parvum* (**Table 1**). To examine the relationship
107 between the protein sequences for the *C. parvum* genes of interest and the top hits of BLASTP
108 analyses, a phylogenetic tree was generated (**Fig 1A**). We found that *cgd3_2540* (H3.1) and
109 *cgd4_3220* (H3.2) closely cluster with histone H3 sequences from other organisms, whereas
110 *cgd4_2030* (CENH3) clustered with other centromeric histone H3 proteins. We then directly
111 compared the amino acid sequences of H3.1 and H3.2 with a global sequence alignment and
112 found that the two sequences were highly similar (99.26%), but less similar compared to the
113 CENH3 (65.10% and 64.43%, respectively) (**Table 2 and Fig 1B**).

114 To further explore the distribution of H3.1 and H3.2 H3 variants, we generated two
115 transgenic lines of parasites that replaced the dispensable thymidine kinase (*tk*) gene with a
116 second copy of *cgd3_2540* (referred to as H3.1-3HA) or *cgd4_3220* (referred to as H3.2-3HA)
117 fused with a triple hemagglutinin (3HA) epitope tag using CRISPR/Cas9 (**Fig 1C, S1 A-B Fig,**
118 **Table S1**). Transgenic parasites were used to infect a human adenocarcinoma cell line (HCT-8)
119 monolayer, cultures were fixed at 18 hours post-infection (hpi) during merogony, stained, and
120 the localization of the 3HA tag was observed by immunofluorescence (IFA) high-resolution
121 confocal laser scanning microscopy equipped with Airyscan detection (LSCM-A). We found that
122 H3.1-3HA (**Fig 1D**) and H3.2-3HA (**Fig 1E**) had a diffuse staining pattern, which was expected
123 based on histone H3 staining in other apicomplexan parasites [27, 45, 46].
124
125 ***The staining pattern of C. parvum centromeric histone H3 (CENH3) is distinct.***
126 To visualize *C. parvum* centromeres, we used CRISPR-Cas9 gene editing to add a 3HA tag to
127 the C-terminus of the centromere-specific histone H3 variant protein (referred to as CENH3-
128 3HA) (**Fig 2A, S2 A-B Fig, Table S1**). After successfully selecting and amplifying these
129 transgenic parasites in immunocompromised mice, we infected HCT-8 cells for 22 h and
130 examined the staining pattern by LSCM-A microscopy. The CENH3 staining pattern observed in
131 *C. parvum* was unexpectedly highly diffuse and looked more like the pattern found in the H3.1-
132 3HA and H3.2-3HA tagged parasites (**Fig 2B-C**). The diffuse pattern of CENH3 staining in *C.*
133 *parvum* contrasts sharply with the regional centromeres previously described in *T. gondii* [27,
134 47]. Hence, we utilized a CENH3-3HA-tagged *T. gondii*, gifted by Dr. Kami Kim, as a staining
135 control for our experiments. These parasites were used for the infection of HCT-8 cells, fixed at
136 24 hpi, stained, and examined by high-resolution LSCM-A immunofluorescence (IFA)

137 microscopy (**Fig 2D-E)**. We found that the staining pattern of the centromeric histone H3 in *T.*
138 *gondii* is punctate, similar to what has been found previously in *T. gondii* by other investigators
139 [27, 47].
140
141 ***Mitosis is synchronous in C. parvum and centromeres remain diffuse.***
142 A vital step in mitosis is centrosome duplication, and previous studies in apicomplexans have
143 shown that it can be traced using antibodies that recognize the centrin 1 protein [27, 48]. A single
144 point adjacent to the nucleus occurs in non-replicating cells, while two centrin 1 positive points
145 per nucleus indicates the parasite is undergoing replication [27, 48]. In *Plasmodium*, during
146 schizogony, asynchronous duplications of centriolar plaques, structural equivalents of
147 centrosomes, have been observed across multiple nuclei within a single cytoplasm [28]. We
148 sought to identify centrosomes in *C. parvum* and determine whether its mitosis occurs
149 asynchronously, like *Plasmodium.* To identify parasites undergoing early mitosis, we infected
150 HCT-8 cells with excysted wild type *C. parvum* sporozoites, washed off uninvaded sporozoites
151 at 2 h, fixed the cultures at various timepoints between 6.5-8.5 hpi, and stained with Hoechst and
152 an anti-centrin-1 antibody. We found that, unlike *Plasmodium*, *C. parvum* appears to undergo
153 synchronized mitosis, as all nuclei within a dividing meront consistently exhibited two centrin-1
154 positive points per nucleus (**Fig 2F**). To determine if the diffuse centromere staining pattern
155 persisted during active mitosis in *C. parvum*, we infected cultures with CENH3-3HA parasites
156 and repeated the experiment previously described. We found that nuclei undergoing mitosis also
157 displayed a diffuse CENH3-3HA staining pattern by LSCM-A (**Fig 2G**). Despite
158 troubleshooting, we could not identify a signal in various CENH3-tagged lines using

159 ultrastructure expansion or immuno-electron microscopy, which may be due to the low
160 abundance of CENH3 and difficulty preserving the epitope.
161
162 ***The telomere (G-strand binding protein, GBP) staining pattern is apical in C. parvum.***
163 G-quadruplex structures readily form at repetitive telomeric sequences and require G-quadruplex
164 binding proteins (GBPs) for stabilization (**Fig 3A**). A previous study identified *cgd1_3530* as the
165 GBP in *C. parvum* and determined the specific sequence necessary for *Cp*GBP binding
166 (GGTTA) [49]. Using AlphaFold and ChimeraX, we modeled the G-quadruplex structure
167 formed by this repetitive sequence and visualized how the *Cp*GBP protein interacts with and
168 stabilizes it. (**Fig 3B**). To identify the location of *C. parvum* telomeres relative to the
169 centromeres, we engineered transgenic parasites to express a 3HA tag at the gene encoding the
170 C-terminus of the G-quadruplex binding protein (referred to as GBP-3HA) (**Fig 3C, S2 A-B Fig,**
171 **Table S1**). Previous studies in *Plasmodium* have found that the telomeres are consistently found
172 on the opposite pole to the centromeres [50-52]. Since the centromeres were located at the apical
173 end of the nuclei in meronts, we expected that *C. parvum* telomeres would be at the basal end.
174 However, LSCM-A microscopy on infected HCT-8 monolayers (24 hpi) revealed that the
175 telomeres were also located at the apical side of the nucleus (**Fig 3D)**.
176
177 ***The telomere (GBP) and centromere (CENH3) staining patterns overlap in C. parvum.***
178 To confirm that *C. parvum* centromeres and telomeres had overlapping nuclear locations, we
179 generated an additional line of transgenic parasites that replaced the dispensable thymidine
180 kinase (*tk*) gene with a second copy of an N-terminally 3HA tagged CENH3 and GBP C-
181 terminally tagged with 3Ty via CRISPR/Cas9, with an intervening P2A split peptide to facilitate

182 co-expression of separate proteins (referred to as 3HA-CENH3-GBP-Ty) (**Fig 3E, S1C-D Fig,**
183 **Table S1)**. HCT-8 cultures were infected with 3HA-CENH3-GBP-Ty parasites, fixed at 6.5 hpi,
184 and examined by LSCM-A microscopy after staining. We confirmed that 3HA-CENH3 and
185 GBP-3Ty staining overlapped completely on the apical end of the nucleus (visualized by
186 Hoechst) (**Fig 3F)**.
187
188 ***Detection of mitotically active DNA, microtubules, and the nuclear pore proteins in C. parvum***
189 The phosphorylation of histone H3 (specifically at serine 10 and serine 28) is a highly conserved
190 mechanism for initiating chromosome condensation in preparation for mitosis [53]. Antibodies
191 recognizing the phosphorylated version of H3 at serine 10 are commonly used in other systems
192 to determine which cells are currently undergoing mitosis from late interphase through telophase
193 [54]. Even though apicomplexan parasites are known not to condense their chromosomes, *C.*
194 *parvum* meronts frequently stained positive for the phosphorylated histone H3 (PH3) antibody
195 (**Fig 4A**). Furthermore, PH3 positive parasites also contained nuclei with duplicated centrin-1
196 positive centrosomes, suggesting that it provides a marker of mitotic parasites. We visualized
197 nuclear pores in *C. parvum* with an antibody that recognizes NUP116 in *Plasmodium falciparum*
198 *(P. falciparum)* and found that it reliably stained the parasite nucleus in a punctate pattern that
199 was concentrated primarily peripherally in the nucleus (**Fig 4B**). Among apicomplexan parasites,
200 mitosis has primarily been studied in *T. gondii* and *P. falciparum* [16, 17, 27, 55]. These studies
201 demonstrate that once centrosomes duplicate, and the nuclear envelope forms a tunnel-like
202 structure, organizing spindle microtubules within it. As the tunnel progressively perforates,
203 spindle microtubules access the centromere, attaching to mediate chromosome movement [32].
204 This process was visualized in *C. parvum* by staining with antibodies that recognize the centrin-1

205 and alpha tubulin (**Fig 4C-D**). We frequently observed two conformations of centrin-1 tubulin
206 structures that may correlate with early (Fig 4C) and late mitotic phases (Fig 4D). Early in
207 mitosis, the microtubules are relatively short and form a straight line (**Fig 4C, E**). Later, they are
208 accompanied by a wider nucleus, have elongated, and form a "v" shape, suggesting they have
209 attached to the chromosomes and are mediating their movement before budding (**Fig 4D, F**).
210

211 ***Composition of centromeres in C. parvum and T. gondii***

212 Centromeres are defined by the deposition of CENH3-containing nucleosomes [27, 56]. Given
213 the diffuse staining of CENH3, we wanted to further characterize the centromere by identifying
214 DNA sites bound by this protein. Therefore, we adopted protocols for CUT&RUN to identify
215 centromeres based on CENH3 binding based on capture with anti-HA antibody in *C. parvum*
216 [44]. To ensure sufficient HA binding, we developed a CENH3 line tagged with spaghetti
217 monster (referred to as CENH3-sm) which contains 10 HA epitope repeats for these experiments
218 and validated identical staining patterns to CENH3-3HA *C. parvum* (**S2 A-C Fig, Table S1**). To
219 validate our experimental strategy, we first applied CUT&RUN to *T. gondii*, whose centromeres
220 have previously been defined by ChIP-seq [27]. Our CUT&RUN data closely matched earlier
221 findings, with CENH3 enrichment observed at discrete chromosomal loci corresponding to the
222 previously described centromeres (**Fig 5A, S3A-C Fig**). We also detected the positive correlation
223 of CENH3 with H3K9me3 and inverse correlation with H3K4me3 reported in earlier ChIP-chip
224 analyses (**Fig 5A, S3A-B Fig**). Based on these signals, we implemented a stepwise strategy to
225 identify centromeric regions. Valleys in H3K4me3, consisting of 20 kb windows, sized to match
226 reported centromere lengths (16 kb ± 3.4 kb)[27], combined with co-enrichment of H3K9me3
227 with CENH3-smHA were used as criteria for identifying centromere regions (**S3D Fig**).

228 Applying these rules, we identified a single centromere in each of the 13 chromosomes of *T.*
229 *gondii* (**S3E Fig**), with Chr VIIb identified as part of Chr VIII [57](**S3C Fig**).
230 We next applied CUT&RUN to *C. parvum*. Initial experiments using a 120-minute MNase
231 digestion failed to generate usable data, as both sequencing depth and genome coverage were
232 low compared to negative controls (**S1 Dataset**). Since CENH3 nucleosomes can be
233 hypersensitive to MNase digestion [58], we tested digestion times of 5, 30, and 60 min. The 30
234 min digestion yielded the best coverage and sequencing depth, and these conditions were used
235 for following analyses (**S1 Dataset, S4A Fig**). Unlike *T. gondii*, read mapping profiles for
236 CENH3 in *C. parvum* showed signals broadly distributed along chromosomes (**Fig 5B**). To
237 locate centromeric regions in *C. parvum*, we first attempted the *T. gondii* stepwise strategy, but
238 no valid windows were detected. As the CENH3 distribution resembled that of the holocentric
239 nematode *Caenorhabditis elegans* (*C. elegans*), we adjusted thresholds accordingly by restricting
240 the peaks analysis to 400 bp windows (**S4B Fig**). We identified 423 CENH3-enriched regions
241 distributed across all chromosomes (**Fig 5C**). Heatmaps and aggregate signal profiles showed
242 that these windows displayed features of CENH3 enrichment correlated with H3K9me3
243 deposition and H3K4me3 depletion, suggesting that they represent centromere-associated
244 chromatin (**Fig 5D-E**). Importantly, these signals were largely absent in wild type parasites
245 stained with HA antibody as a control, supporting their authenticity (**Fig 5D-E**). To further refine
246 localization, we excluded windows overlapping with WT-HA signals, reducing the dataset to 347
247 high-confidence centromeric windows (**S4C Fig**). Taken together, these results indicate that *C.*
248 *parvum* possesses many small CENH3 sites dispersed across eight chromosomes, in contrast to
249 the monocentric nature of *T. gondii*.

250 We further investigated characteristics of *C. parvum* centromeres. In contrast to *T. gondii*,
251 where centromeres are typically located within large intergenic regions, no extended intergenic
252 regions were observed in *C. parvum* (**S4D Fig)**. Comparison of intergenic regions in *C. parvum*
253 revealed that they are on average ~400-500 bp in length compared to ~1,5 to 2 kb in *T. gondii*
254 (Fig 4D). Moreover, the size of the largest single intergenic region in each *C. parvum*
255 chromosome was limited to ~2,5 – 8 kb compared to ~10-90 kb in *T. gondii*. Centromeres in *T.*
256 *gondii* were associated with one of these large intergenic regions, while no pattern was seen
257 between the CENH3 signal and large intergenic islands in *C. parvum* (**S4D Fig**). To assess
258 sequence properties of *C. parvum* centromeric windows, motif analysis of *C. parvum*
259 centromeric windows was performed using MEME, revealing two GA-rich motifs enriched at
260 CENH3-associated sites (**Fig 5F**). The distribution and clustering of these repeats varied across
261 the 8 chromosomes and some regions contained a single GA repeat, while others contained
262 multiple repeats (**Fig 5F**). Surprisingly, the GA repeats extended into gene coding regions rather
263 than being restricted intergenic regions (**Fig 5F, S4D Fig**).
264

265 **DISCUSSION**

266 Despite rapid asexual proliferation being required for parasite expansion, the molecular
267 mechanisms that underlie *C. parvum* mitosis have remained unexplored. To investigate this
268 process, we examined nuclear division using markers to track multiple rounds of mitosis during
269 merogony. Nuclear division in *C. parvum* occurs synchronously as shown by staining with
270 phospho-H3 and centrin-1, which provide markers for mitotically active chromatin and
271 duplicating centrosomes, respectively. Surprisingly, both CENH3, a marker for centromeres, and
272 GBP, a marker for telomeres, were diffusely localized across the apical half of the nucleus.

273 Moreover, these diffuse apical patterns persisted throughout mitosis, as shown by tracking
274 nuclear division through stages visualized with centrin-1 and microtubules. To explore the
275 molecular nature of centromeres, we performed CUT&RUN sequencing of transgenic parasites
276 expressing epitope-tagged CENH3. Although discrete monocentric peaks were detected in the
277 related parasite *T. gondii*, CENH3 binding sites were diffusely scattered across ~ 350 sites in the
278 *C. parvum* genome. Overall, these findings indicate that *C. parvum* has evolved an alternative
279 chromosome structure compared to other apicomplexan parasites, differences that likely have
280 significant functional consequences for chromosome stability, meiotic recombination, and
281 speciation.

282 Following entry of sporozoites (or merozoites) into the host cell, the parasite undergoes
283 merogony, consisting of 3 rounds of nuclear division prior to cytokinesis to generate infectious
284 merozoites. By tracking nuclear division with phospho-H3, to detect mitotically active nuclei,
285 and centrin-1 to monitor dividing centrosomes, we observed that all nuclei found in a common
286 cytoplasm shared the same centrin-1 staining pattern (whether dividing or not), indicating that
287 nuclei divide synchronously. This pattern differs from *Plasmodium* schizogony, where nuclei are
288 observed at different mitotic stages within a single schizont [28]. In *Plasmodium*, nuclear pores
289 are important for cell division as they facilitate the transport of mitotic molecules through the
290 intact nuclear envelope and associate with the centriolar plaques [31, 59]. Although we did not
291 examine the dynamics of nuclear pores during division, they appear as peripheral puncta in
292 mature meronts and may serve a similar function in *C. parvum*. Staining with alpha-tubulin
293 allowed us to visualize *C. parvum* microtubules during mitosis, particularly at early stages where
294 it spanned dividing nuclei, likely representing extra-nuclear spindles involved in chromosome
295 separation. By monitoring the duplication of the centrosomes, distance between the centrin-1

296 foci, length of microtubules, and elongation of the nucleus we generated a pseudo timeline for
297 early, mid, and late merogony. These findings provide an important foundation for studies of the
298 dynamics of centromere staining described below.

299 Unexpectedly, we found a diffuse nuclear CENH3-3HA staining pattern rather than the
300 punctate pattern observed in other apicomplexan parasites [27, 29, 35]. We also confirmed that
301 the diffuse CENH3 staining pattern did not deviate when the method of tagging was altered (e.g.
302 GFP, mNeon, and smHA), when the location of the tag was swapped (C vs N-terminally tagged),
303 or when a tagged second copy of the gene was inserted into a neutral locus of the genome. We
304 also developed epitope-tagged lines of telomere-binding protein GBP, similar to studies in
305 *Eimeria* and *Plasmodium* [60, 61]. Unlike in other apicomplexans, GBP also showed an apical
306 location in *C. parvum*, overlapping closely with CENH3 [18-20, 50]. We further confirmed that
307 the telomeres and centromeres occupied a similar nuclear location using a parasite strain in
308 which CENH3 and GBP proteins were simultaneously expressed as tagged second copies. This
309 pattern contrasts sharply with other apicomplexans where telomers are localized to the opposite
310 pole of the nucleus from centromeres [50-52]. We sought to determine if centromeres remained
311 diffuse throughout mitosis by simultaneously visualizing the centriole-equivalent structures and
312 centromeres by staining CENH3-3HA with anti-HA and centrin-1 antibodies. We confirmed that
313 in *C. parvum,* the diffuse centromere staining pattern does not change throughout mitosis, which
314 further contrasts with the highly focal nature of centromeres in *T. gondii* and *P. falciparum* [26,
315 27].

316 Given the highly unusual staining patterns of CENH3 in *C. parvum*, we decided to
317 investigate CENH3 binding sites on DNA using CUT&RUN sequencing. For comparison, we
318 also performed CUT&RUN studies on CENH3 in the related parasite *T. gondii* and compared

319 them to previous studies that used ChIPSeq to define centromeres [27]. In *T. gondii*, CUT&RUN
320 sequencing identified highly similar CENH3 binding sites to those reported previously by
321 ChIPSeq [27] with a single predominant peak on each chromosome, including newly defined
322 peaks on chromosome IV, that had not been identified previously. Centromeres in *T. gondii*
323 consist of gene-poor regions of ~15 kb that are not defined by any particular sequence or repeats
324 but instead are positively correlated with H3K9me3 and inversely correlated with H3K4me3,
325 typical chromatin patterns expected for centromeric regions [18, 27]. Under similar conditions,
326 CUT&RUN experiments for CENH3 binding sites in *C. parvum* failed to identify similar
327 singular dominant peaks on each chromosome. Instead, CENH3 binding sites were
328 hypersensitive to MNase digestion, with the signal being the highest at a 30- min incubation
329 time, similar to that observed in ChIP-seq studies of the holocentric nematode *Caenorhabditis*
330 *elegans* (*C. elegans*) [56]. Under optimal digestive conditions, we found that the CENH3 signal
331 in *C. parvum* was broadly distributed along chromosomes, with ~ 350 distinct sites scattered
332 across 8 chromosomes. Interestingly, like *T. gondii*, *C. parvum* CENH3 peaks also correlated
333 with H3K9me3 signal and were found in areas lacking H3K4me3, consistent with a centromere-
334 associated chromatin pattern. The distribution of CENH3 binding sites in *C. parvum* is similar to
335 that described in *C. elegans* as polycentric, implying that CENH3 binds to distinct sites rather
336 than diffusely across the entire chromosome [56].

337 Collectively, our findings are consistent with *C. parvum* containing holocentric centromeres
338 based on the following criteria: Firstly, the staining pattern of CENH3 diffusely stains the apical
339 half of the nucleus under nondividing conditions, in contrast to the focal staining of CENH in *T.*
340 *gondii* [18, 27] and *P. falciparum* [26]. Secondly, the diffuse pattern of CENH3 staining remains
341 throughout mitosis, suggesting centromeres do not coalesce into a single regional center. Thirdly,

342 CENH3 binding sites as defined by CUT&RUN resemble the dispersed pattern of low-intensity
343 peaks seen in *C. elegans*, which has well-characterized holocentric chromosomes. Finally, the
344 CENH3 binding sites show evidence of simple nucleotide repeats, a feature also seen in some but
345 not all forms of holocentric chromosomes [62]. One unusual feature of the GA repeat is that they
346 extend into coding regions, a feature also described in *Schizosaccharomyces pombe* [63] and
347 *Candida albicans* [64] neocentromeres that occur in regions that are transcriptionally active but
348 characterized by lower gene expression.

349 Holocentric chromosomes have been documented in at least 768 species, primarily through
350 direct cytological observation, yet its functional implications and evolutionary origins remain
351 poorly understood [38, 56, 65, 66]. Current evidence suggests that holocentric chromosomes
352 have evolved convergently at least 13 times across distantly related taxa in both the plant and
353 animal kingdoms [37, 38, 66]. Holocentricity has not previously been described in protists, and
354 hence it likely evolved independently in *C. parvum*. One proposed advantage of holocentricity is
355 its capacity to stabilize chromosomal fragments during mitosis, thereby mitigating genetic loss.
356 This trait may confer a selective benefit to organisms frequently exposed to elevated levels of
357 DNA damage due to environmental stressors or lifestyle factors [37, 65]. Thus, holocentricity
358 may impart genome stability under stress encountered in the gastrointestinal system where the
359 parasite is exposed to toxic bacterial metabolites [67] and host immune responses [68]. Despite
360 this potential advantage, holocentricity also presents a major challenge for coordinating
361 chromosome segregation following crossover during meiosis I. Well-characterized holocentric
362 species have evolved mechanisms to circumvent this issue, such as inverted meiosis or, in the
363 case of *C. elegans*, the deployment of kinetochore proteins that localize to discrete chromosomal
364 regions, effectively mimicking monocentric behavior [69]. Whether *C. parvum* uses a similar

365 mechanism as *C. elegans* to localize kinetochore proteins to discrete sites on the chromosome is
366 uncertain, but previous work from our laboratory examining crossover rates during *C. parvum*
367 meiosis revealed a high frequency of crossover events but failed to find evidence for inverted
368 meiosis [70]. Collectively, these findings suggest that *C. parvum* has evolved a holocentric
369 chromosome architecture that may also involve a distinct meiotic mechanism that underlies its
370 propensity for speciation.

371 **Limitations and Future Studies**

372 Examination of the nuclear organization of *C. parvum* throughout the cell cycle revealed a
373 persistently diffuse centromere staining pattern, suggesting a holocentric chromosome structure.
374 During division, such multiple centromeric sites dispersed along the chromosome are expected to
375 bind centrosomes and thereby connect to microtubules for chromosome separation. Although we
376 visualized these events in a pseudo-timeline, future studies using fluorescent reporters could
377 potentially provide more precise information on the formation of centrosomes, coordinated
378 assembly of microtubules, and nuclear division in *C. parvum*. However, obtaining direct
379 cytological data in support of holocentric centromeres and their behavior during nuclear division
380 will be challenging in this system because chromosomes do not condense during division.
381 Alternatively, it may be possible to explore the nature of centromeres by examining the
382 distribution of other conserved kinetochore binding proteins during nuclear division. Such
383 studies could shed further light on chromosome tethering in nuclear division and provide
384 invaluable insights into unique evolutionary adaptations in *C. parvum*.

385

386 **Acknowledgements:**

387 We thank Jennifer Barks for assistance with cell culture, Dr. Wandy L. Beatty, Microbiology
388 Imaging Facility, Washington University School of Medicine in St. Louis, for assistance with
389 microscopy, and Dr. Kami Kim, Univ. South Florida, for providing the *T. gondii* CENH3-HA
390 line used here. We are grateful for helpful comments from Drs. Danial E Goldberg, Douglas L.
391 Chalker, and Tim Schedl, Washington University and Dr. Lihua Xiao, South China Agricultural
392 University. Genome sequencing was performed by the GTAC Genome core at Washington
393 University in St Louis. Supported in part by the Graduate Research Fellowship Program,
394 National Science Foundation (to A.K.) and grant AI175150 from the National Institutes of
395 Health (to L.D.S.).
396

397 **Author contributions**

398 AK: Conceptualization, Data curation, Formal analysis, Funding acquisition, Investigation,
399 Methodology, Resources, Validation, Visualization, Writing – original draft, Writing – review &
400 editing
401 WH: Data Curation, Formal analysis, Investigation, Methodology, Resources, Visualization,
402 Writing
403 MK: Investigation, Methodology, Resources
404 LFJ: Investigation, Methodology, Resources
405 LDS: Conceptualization, Funding acquisition, Methodology, Project administration, Resources,
406 Supervision, Validation, Writing – original draft, Writing – review & editing
407

408 **Data Sources and Availability:**

409 All materials described here are available from the corresponding author based on MTA.
410 Sequence for the CUT&RUN analyses have been deposited to the NCBI Bioproject #
411 PRJNA1330822.
412 **Declarations:**
413 The authors declare that they have no conflicts to disclose.
414
415 **MATERIALS & METHODS**
416 **Animal studies and ethical approval.**
417 Animal studies were approved by the Institutional Animal Studies Committee (School of
418 Medicine, Washington University in St. Louis). *Ifngr1*$^{-/-}$ mice (003288; Jackson Laboratories),
419 and NOD scid gamma mice (referred to as NSG) (005557; Jackson Laboratories) were bred in-
420 house in a specific-pathogen-free animal facility on a 12:12 light-dark cycle. Male and female
421 mice between 8 and 12 weeks of age were used for sex-matched groups used in crossing
422 experiments. Mice were co-housed with siblings of the same sex throughout the experiments.
423 **Cell culture.**
424 HCT-8 cells (Human ileocecal adenocarcinoma, ATCC CCL-244) derived from a human
425 ileocecal carcinoma were cultured in RPMI 1640 ATCC Modification medium supplemented
426 with 10% fetal bovine serum at 37 °C in a 5% CO_2 incubator. After trypsinization, 450,000 cells
427 were plated on glass coverslips in 24-well plates and used for experiments. Cells were confirmed
428 to be mycoplasma-free with the e-Myco plus Mycoplasma PCR detection kit.
429 **Immunofluorescence assays & microscopy.** Staining protocols have been previously described
430 and all antibodies are listed in **Table S2** [71]. Briefly, infected HCT-8 cultures were fixed with
431 4% formaldehyde 8-24 hours post-infection (hpi), permeabilized with 0.1% Triton X-100,

432 blocked with 1% bovine serum albumin (BSA), stained with a primary antibody mixture for 1 h
433 followed by secondary antibodies for 1 h and Hoechst for 20 min. Primary antibodies were
434 diluted for staining: anti-HA (rat, 1:500), VVL-Biotin (*Vicia Villosa* Lectin, Biotinylated, 1:500),
435 anti-Aldolase (ALD, rabbit, 1:1000) centrin-1 (mouse, 1:250), anti-Ty (mouse, 1:250), and anti-
436 PH3 (rabbit, 1:500). All Alexa Fluor secondary antibodies were diluted at 1:1000 and Hoechst
437 was diluted 1:2000. Coverslips were mounted onto microscope slides with Prolong Glass
438 Antifade Mountant. Coverslips were visualized using a Zeiss LSM880 laser scanning confocal
439 microscope equipped with a 63x, 1.4 N.A. Zeiss Plan Apochromat oil objective lens and Airy
440 scan. Images were acquired with ZEN v2.1, v2.5 software and further analyzed using ImageJ.
441

442 **CRISPR/Cas9 plasmid construction.**

443 ***Plasmid construction***

444 Primers used to generate the following plasmids were ordered from IDT and all sequences are
445 found in **Table S3**. SnapGene (v7.1.1) and NEBuilder Assembly Tool (v2.9.0) were used to
446 construct plasmid maps and design primers.

447 The CENH3-3HA tagging plasmid was generated using the previously described ABC-3HA
448 tagging plasmid [72] by replacing the C-terminal and 3'UTR sequences with equivalent regions
449 from the *Cp*CENH3 gene amplified from *C. parvum* cDNA to generate the tagging plasmid
450 CENH3-3HA-Nluc-P2A-Neo^{R}.

451 The 3HA-CENH3- GBP-3Ty tagging plasmid was created via a seven-way Gibson assembly
452 combining a backbone generated from the TK-GFP-Nluc-P2A-Neo^{R}-TK homology tagging
453 plasmid previously generated in our lab [73] together with the following fragments: 1) The 5'
454 homology region of CENH3 (500 bp), the CENH3 CDS, a portion of the 3' homology region of

455 CENH3 (216 bp) were amplified from the CENH3-3HA tagging plasmid described above. 2)
456 The 3HA-pLinker region was amplified from a TK-3HA-CENH3-Nluc-P2A-Neo^{R}-TK plasmid
457 (data not shown in this study), 3) the GBP CDS was amplified from *C. parvum* genomic DNA,
458 4) the pLinker-3Ty sequence was amplified from a tagging plasmid previously generated in our
459 lab [72], and 5) the P2A skip peptide sequence was generated as a gBlock Gene Fragment from
460 Azenta. The U6:sgTK plasmid previously generated in our lab was utilized for all experiments
461 with TK locus replacement repair plasmids [73].
462 The H3.1-3HA and H3.2-3HA tagging plasmids were generated via Gibson assembly using
463 the 3HA-CENH3-GBP-3Ty plasmid to provide a backbone, the pLinker-3HA region was
464 amplified from the CENH3-3HA tagging plasmid described above, and the CDS regions for
465 H3.1 and H3.2 were amplified from *C. parvum* genomic DNA.
466 The GBP-3HA tagging plasmid was generated using the CENH3-3HA tagging plasmid
467 described above for the backbone and replacing the C-terminal and 3'UTR sequences with the
468 GBP CDS sequence amplified from *C. parvum* genomic DNA.
469 CENH3 and GBP CRISPR/Cas9 plasmids were created via Gibson assembly of the
470 linearized backbone amplified from the TK CRISPR/Cas9 plasmid (Addgene 122852) and an
471 oligonucleotide with the sgRNA specific for the CENH3 or GBP gene [73]. The Eukaryotic
472 Pathogen CRISPR guide RNA/DNA Design tool (http://grna.ctegd.uga.edu) was used to identify
473 CENH3 and GBP sgRNA sequences.
474 **Amplifying transgenic parasites in mice.**
475 The transfection and amplification of parasites in immunocompromised mice were conducted as
476 previously described [73-76]. Briefly, $1x10^{8}$ freshly excysted sporozoites were electroporated
477 with 100 µg of repair plasmid and 66 µg of CRISPR/Cas9 plasmid, then resuspended in 300 µL

478 of cold DPBS. *Ifngr1*$^{-/-}$ mice were first orally gavaged with an 8% (wt/vol) sodium bicarbonate
479 solution to neutralize stomach acid, followed by the administration of the electroporated
480 sporozoites. To facilitate the selection of transgenic parasites, paromomycin (16 g/L) was
481 provided in the drinking water 24 h post-infection. Fecal pellets were collected at intervals post-
482 infection for luciferase assays and diagnostic PCR analysis to verify parasite growth and proper
483 gene insertion. Oocysts were isolated from fecal material using bleach treatment, and 20,000
484 oocysts per mouse were employed for a subsequent round of amplification in NSG mice.
485 **Luciferase assays for mouse experiments.** Fecal samples collected from infected mice were
486 analyzed with the Promega Nano-Glo luciferase assay kit, as previously described [76]. The
487 luciferase activity was measured using the BioTek Cytation 3 cell imaging multi-mode reader.
488 The number of relative luminescence units per milligram of feces was obtained by dividing the
489 average values from two technical replicates by the fecal sample weight.
490 **Quantifying oocyst shedding in mouse experiments.** DNA was extracted from fecal pellets
491 collected from infected mice using the QIAamp PowerFecal DNA kit, following previously
492 established methods [73, 75, 76]. Quantitative PCR (qPCR) analysis was conducted to determine
493 the number of oocysts at each time point based on *C. parvum* glyceraldehyde-3-phosphate
494 dehydrogenase (GAPDH) primers and a standard curve derived from a dilution series (**S2 Table**)
495 [73]. Genomic DNA (gDNA) amounts were quantified using the QuantStudio 3 real-time PCR
496 system.
497 **Confirmation of insertions in transgenic parasites by PCR.**
498 To confirm the correct integration of the homology repair template, extracted gDNA from
499 murine fecal samples and wild type controls were used as the template. PCR amplification was
500 performed using 1 μL of the extracted gDNA, Q5 Hot Start high-fidelity 2X master mix or

501 PrimeSTAR GXL premix (TaKaRa), and primers at a final concentration of 500 nM on a Veriti
502 96-well thermal cycler. All PCR products were resolved on a 1% agarose gel containing GelRed
503 (1:10,000) and visualized using the ChemiDoc MP imaging system.

504 **Oocyst purification from fecal material and storage.**

505 The *C. parvum* isolate AUCP -1 used for transfections was purified from fecal material collected
506 from male Holstein calves at the University of Illinois at Urbana-Champaign [77]. All
507 procedures involving the calves received approval from the Institutional Animal Care and Use
508 Committee (IACUC). Transgenic oocysts were purified in-house from fecal material collected
509 from NSG mice, using a saturated sodium chloride solution for oocyst flotation [78]. Post-
510 purification, oocysts were stored at 4°C in phosphate-buffered saline (PBS) for up to three
511 months following fecal collection.

512 **Structural predictions**

513 The protein structure of the G-quadruplex binding protein (GBP, *cgd1*_3530) was predicted
514 using Alphafold 3 (www.alphafoldserver.com). Using ChimeraX
515 (https://www.cgl.ucsf.edu/chimerax/), we modeled how the G-quadruplex structure formed by
516 the *Cp*GBP repetitive binding sequence (GGTTA) [49] interacts and is stabilized by the CpGBP
517 protein.

518 **Parasite Preparation and Lysis for CUT&RUN experiments.**

519 The CENH3-3HA line of *T. gondii* [27] was obtained from the laboratory of Dr. Kami Kim at
520 University of South Florida. *Tg*CENH3-3HA tachyzoites were propagated in human foreskin
521 fibroblasts and harvested using established protocols [79]. *C. parvum* sporozoites ($4x10^7$) and *T.*
522 *gondii* tachyzoites ($1x10^7$) were centrifuged at 2,500 RPM for 5 min, supernatants removed, and
523 parasites were resuspended in 2 mL of cold parasite lysis buffer (10 mM HEPES pH 7.9, 1.5 mM

524 MgCl2, 10 mM KCl, 0.65% NP40 (supplemented with IGEPAL) and 0.5 mM PMSF
525 (supplemented with cOmplete EDTA free protease inhibitor cocktail and sterile distilled H_2O),
526 incubated for 10 min on ice, and centrifuged at 3,000 RPM for 10 min at 4°C (previously
527 described in [80, 81]).

528 **CUT&RUN Processing, Library Preparation, Quality Control & Sequencing.**

529 Following lysis treatment, the lysis buffer was removed, and the nuclei pellet was washed
530 following the CUT&RUN Kit Version 4 protocol (EpiCypher, Inc, Catalog No. 14-1048).
531 Isolated nuclei were incubated with either 1.0 µg of rat anti-HA antibody, 0.5 µg of rabbit anti-
532 H3K4me3 positive control antibody, or 0.5 µg of mouse anti-IgG negative control antibody.
533 Chromatin digestion and release steps were performed according to the EpiCypher protocol, and
534 5 ng of CUT&RUN enriched DNA was used for library preparation according to the CUT&RUN
535 Library Prep Kit User Manual Version 1.5 (EpiCypher, Inc, Catalog No. 14-1001). The
536 concentrations of CUT&RUN library samples were determined via Qubit and quality control
537 were assessed with an Agilent 4200 TapeStation.

538 **CUT&RUN Analysis & Visualization.**

539 Multiple CUT&RUN runs were preformed to obtain biological replicates of each sample. DNA
540 products were sequenced on an Illumina NovaSeq 6000 using 150-bp paired-ends at the GTAC
541 sequencing core at Washington University in St. Louis. Sequence reads obtained from Illumina
542 were trimmed for adapter sequences and poor sequence quality (phred score < 25 and trimmed
543 length < 50) using fastp v0.23.4. The trimmed reads were mapped to the reference *C. parvum*
544 IOWA-CDC genome using BWA-MEM v0.7.17 [82]. Duplicate reads were marked and
545 removed in the bam files using the MarkDuplicates algorithm of picard v3.1.1
546 (https://broadinstitute.github.io/picard/) with REMOVE_DUPLICATES=true,

547 CREATE_INDEX=true, and ASSUME_SORTED=true. Reads with mapping lengths less than
548 50 bp were further removed from the bam files using SAMtools v1.7
549 (http://samtools.sourceforge.net/). Genome coverage and sequence depth were estimated using
550 the mpileup algorithm of SAMtools. The read depth of each locus was normalized by dividing by
551 the total number of counts for all loci, then scaled by multiplying by the number of loci in the
552 genome. Input counts were subtracted from negative control counts. Data was visualized by a R
553 package 'ggplot2' (https://www.rdocumentation.org/packages/ggplot2). Motifs within
554 centromeric windows were identified using MEME v5.5.8 (https://meme-
555 suite.org/meme/tools/meme). Chromosomal distributions of intergenic regions, centromeric
556 windows, and motifs were visualized with Circos plot generated in TBtools-II v2.311
557 (https://github.com/CJ-Chen/TBtools-II).
558
559

560

561 **FIGURES AND LEGENDS**

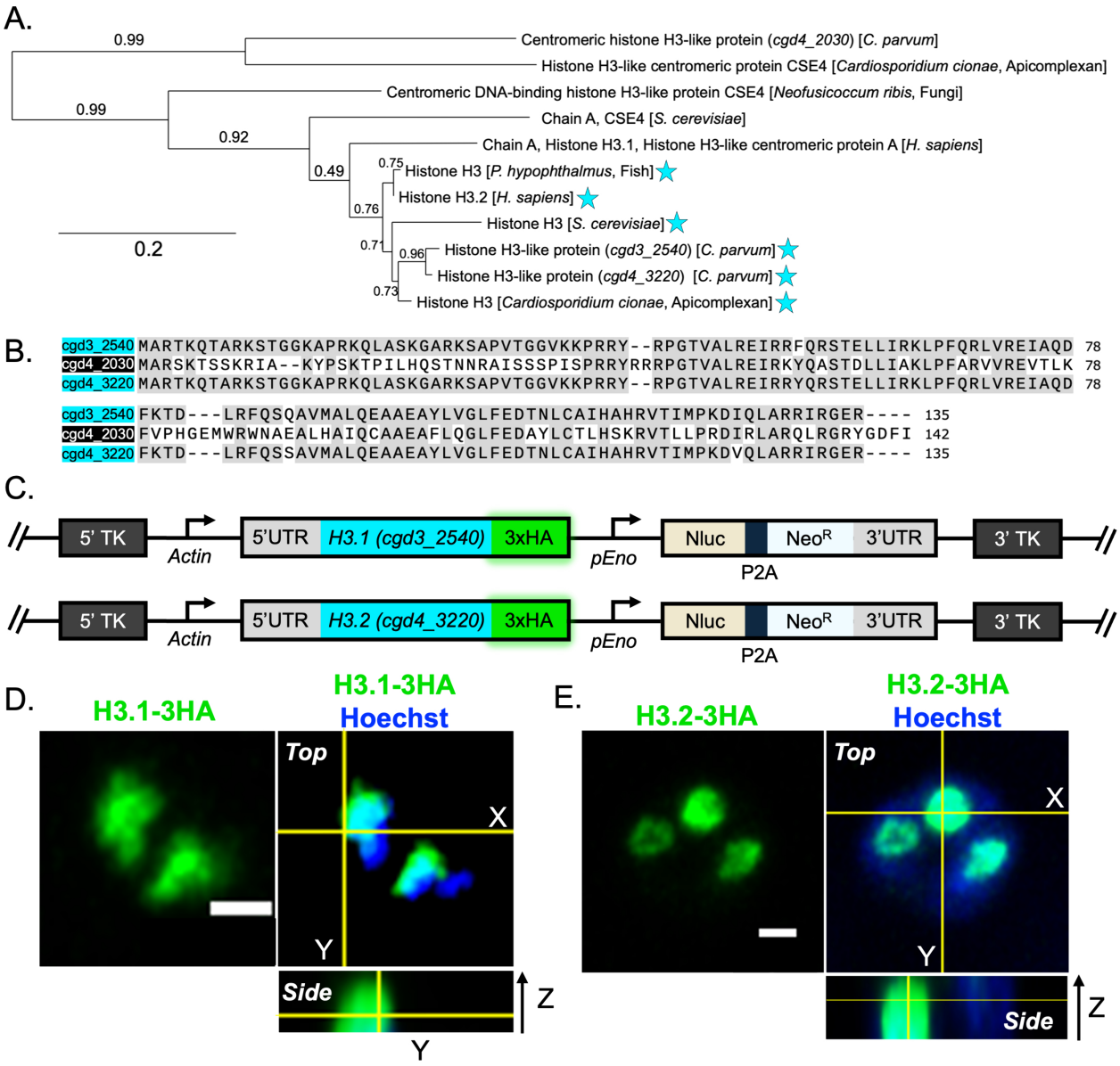

562

563 **Figure 1: Characterization of centromeric histone H3 (CENH3) and histone H3 candidates**

564 **in *C. parvum* and construction of Histone H3-3HA tagged strains**. (A) Phylogenetic

565 relationship of *C. parvum* H3 and centromeric H3 (CENH3) histones and their corresponding top

566 BLASTP hits in other eukaryotes, apicomplexan parasites, *Saccharomyces cerevisiae*, or *Homo*

567 *sapiens*. Cyan stars represent annotated histone H3 genes. (B) Protein sequence alignment of H3

568 (cyan) and CENH3 (black) in *C. parvum*. Amino acids that are identical between at least two
569 sequences are highlighted in grey. (C) Diagram of the targeting constructs designed to replace
570 the endogenous *tk* locus with a second copy of either of the genes annotated as Histone H3-like
571 proteins in *C. parvum* (*cgd3_2540* or *cgd4_3220*), a 3HA tag, and a Nluc-P2A-NeoR cassette.
572 (D) Immunofluorescence staining of transgenic H3.1-3HA or (E) H3.2-3HA parasites. HCT-8
573 cells were infected with transgenic oocysts, fixed at 18 hpi, and stained with rat anti-HA and
574 VVL-Biotin, followed by secondary antibodies Alexa Fluor 488 goat anti-rat IgG and Alexa
575 Fluor 647 Streptavidin. Hoechst was used for nuclear staining. Images were acquired as Z-stacks
576 using a Zeiss LSM-880 Laser Scanning Confocal microscope equipped with Airyscan (LSCM-
577 A) and are presented with orthogonal views. Scale bars, 1 µm.

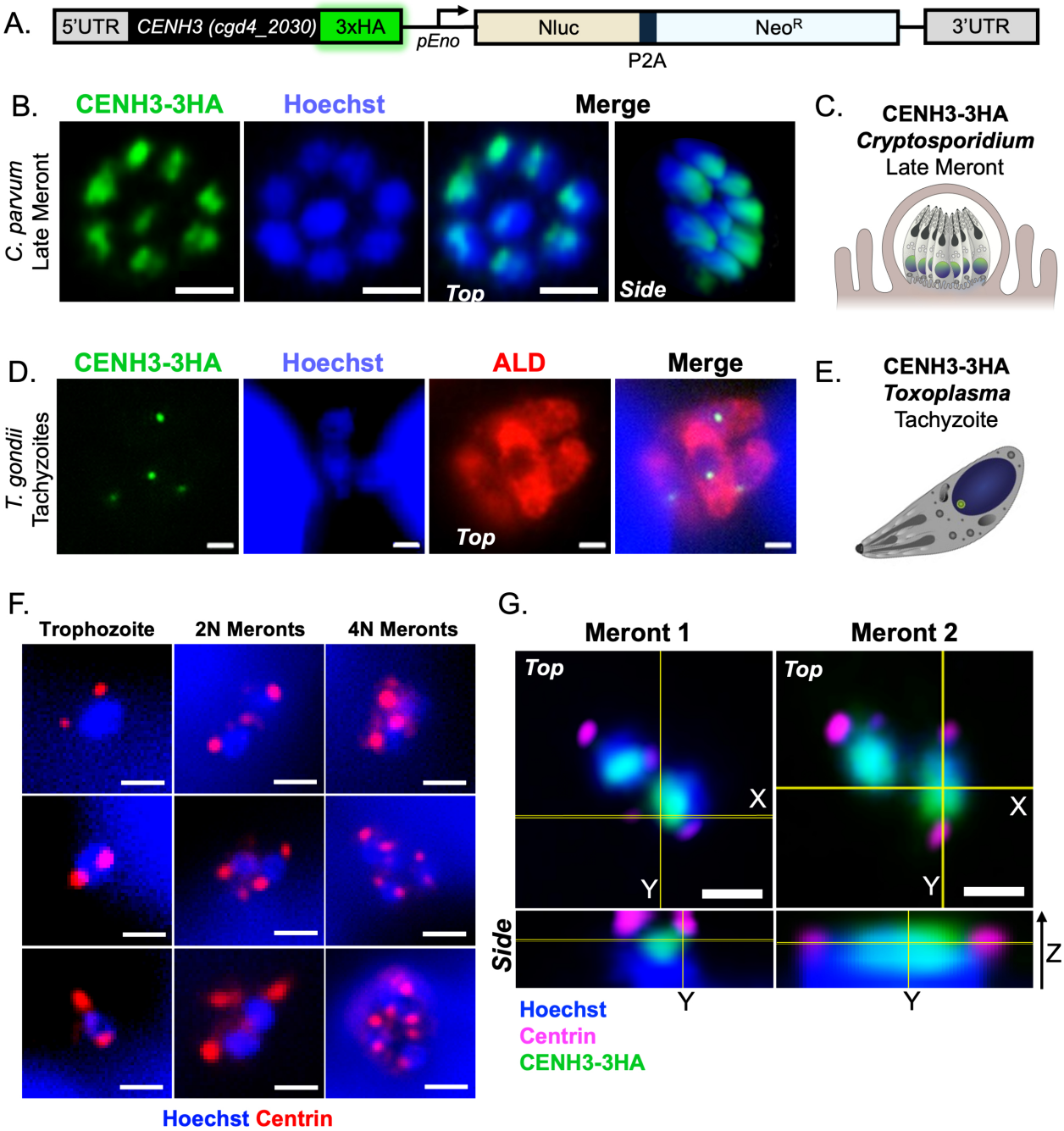

Figure 2. The staining pattern of *C. parvum* centromeric histone H3 (CENH3) is distinct from *Toxoplasma* and remains diffuse during mitosis. (A) Diagram of the targeting construct designed to add a 3HA tag and Nluc-P2A-Neo^R cassette to the C-terminus of the *C. parvum* CENH3 (*cgd4_2030*). (B) HCT-8 cells were infected with CENH3-3HA *C. parvum* parasites, fixed at 22 hpi, and stained with rat anti-HA and VVL-Biotin, followed by secondary antibodies

584 Alexa Fluor 488 goat anti-rat IgG and Alexa Fluor 647 Streptavidin followed by Hoechst
585 staining. Images were acquired as Z-stacks using LSCM-A and are presented with orthogonal
586 views. Scale bars, 1 µm. (C) Cartoon depiction corresponding to the microscopy image in panel
587 (B). In *Cryptosporidium*, a late-stage meront contains eight nuclei that have recently completed
588 cytokinesis to form mature merozoites. The CENH3-3HA signal within each nucleus displays a
589 diffuse staining pattern in *C. parvum*. (D) HCT-8 cells were infected with CENH3-3HA *T.*
590 *gondii* parasites, fixed at 24 hours post-infection (hpi), and stained with rat anti-HA and rabbit
591 anti-aldolase (ALD) to visualize the cytosol, followed by secondary antibodies Alexa Fluor 488
592 goat anti-rat IgG and Alexa Fluor 568 anti-rabbit IgG. Hoechst was used for nuclear staining.
593 Images were acquired as Z-stacks using LSCM-A and are presented with orthogonal views.
594 Scale bars, 1 µm. (E) Cartoon depiction corresponding to the microscopy image in panel (D). In
595 *T. gondii* tachyzoites, the CENH3-3HA signal within each nucleus displays a discrete staining
596 pattern. (F) HCT-8 cells were infected with excysted *C. parvum* sporozoites for 2 h, then washed
597 twice to remove extracellular parasites. Cultures were fixed at 30 min increments between 6-9
598 hpi to identify the first (trophozoites with one nucleus), second (early meronts with 2 nuclei), and
599 third (mid-stage meronts with 4 nuclei) mitotic divisions during the first round of merogony by
600 widefield microscopy. Scale bars, 1 µm. (G) Cultures were infected with CENH3-3HA *C.*
601 *parvum* sporozoites for 2 h, washed, and fixed at 6.5 hpi to capture the first round of mitosis.
602 Cultures were stained with rat anti-HA, rabbit anti-centrin-1, and VVL-Biotin, followed by
603 secondary antibodies Alexa Fluor 488 goat anti-rat IgG, Alexa Fluor 568 goat anti-mouse IgG,
604 and Alexa Fluor 647 Streptavidin, and lastly Hoechst. Parasites undergoing mitosis were
605 identified by having two centrin-1 points per nucleus, whereas parasites in interphase had only

606 one centrin-1 point. Images were acquired as Z-stacks using LSCM-A and are presented with

607 orthogonal views. Scale bars, 1 µm.

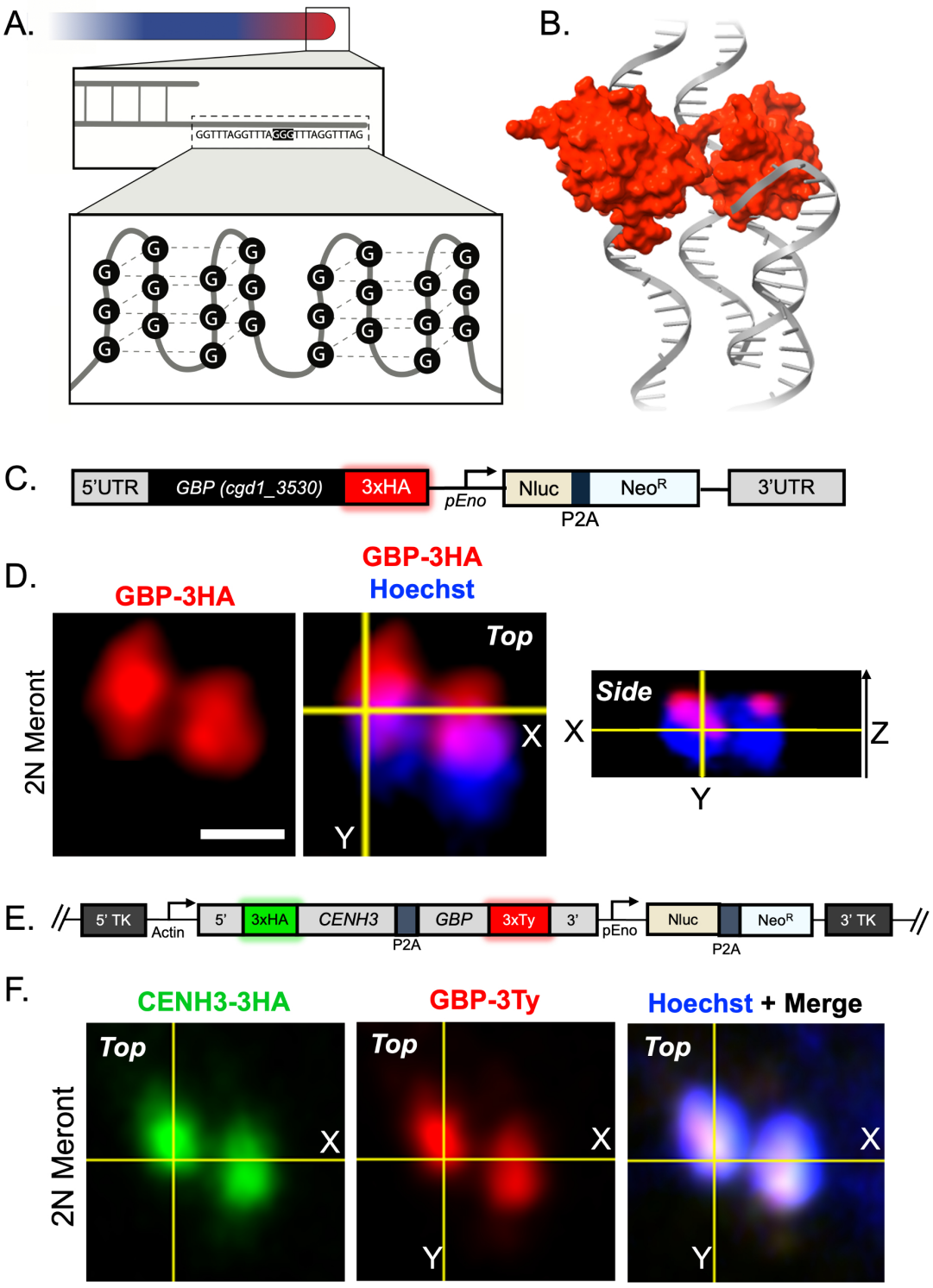

608

609 **Figure 3: The telomere (G-strand binding protein, GBP) staining pattern is apical in *C.***
610 ***parvum* and overlaps with the centromere (CENH3) staining pattern.** (A) The 3' overhang
611 single-stranded DNA at the end of telomeres contains repetitive sequences $(GGTTTA)_n$ in *C.*
612 *parvum* that form G-quadruplex structures. (B) The G-quadruplex binding protein (GBP) is
613 essential for forming and stabilizing these structures. The sequence of *Cp*GBP and its binding
614 motif has been previously determined and the protein structure is modeled by Alphafold and
615 ChimeraX [49]. (C) Diagram of the targeting construct designed to add a 3HA tag and Nluc-
616 P2A-Neo^R cassette to the C-terminus of the G-quadruplex binding proteins gene *(*GBP*,*
617 *cgd1_3530)* (D) HCT-8 cells were infected with GBP-3HA parasites, fixed at 6.5 hpi to capture
618 early meronts (2 nuclei), and stained with rat anti-HA and VVL-Biotin, followed by secondary
619 antibodies Alexa Fluor 488 goat anti-rat IgG and Alexa Fluor 647 Streptavidin. Hoechst was
620 used for nuclear staining. Images were acquired as Z-stacks using LSCM-A and are presented
621 with orthogonal views and the scale bar is 1 µm. (E) Diagram of the targeting construct designed
622 to replace the endogenous *tk* locus with a second copy of CENH3 N-terminally tagged with 3HA
623 and GBP with a C-terminal 3xTy tag separated with a P2A split peptide. (F)
624 Immunofluorescence staining of transgenic 3HA-CENH3-GBP-3Ty parasites. HCT-8 cells were
625 infected with transgenic oocysts, fixed at 6.5 hpi to capture early meronts (2 nuclei), and stained
626 with rat anti-HA, mouse anti-Ty, and VVL-Biotin followed by a secondary antibody stain
627 containing Alexa Fluor 488 goat anti-rat IgG, Alexa Fluor 568 goat-anti mouse, and Alexa Fluor
628 647 Streptavidin. Hoechst was used for nuclear staining. Images were acquired as Z-stacks using
629 LSCM-A and are presented with orthogonal views. Scale bars, 1 µm.

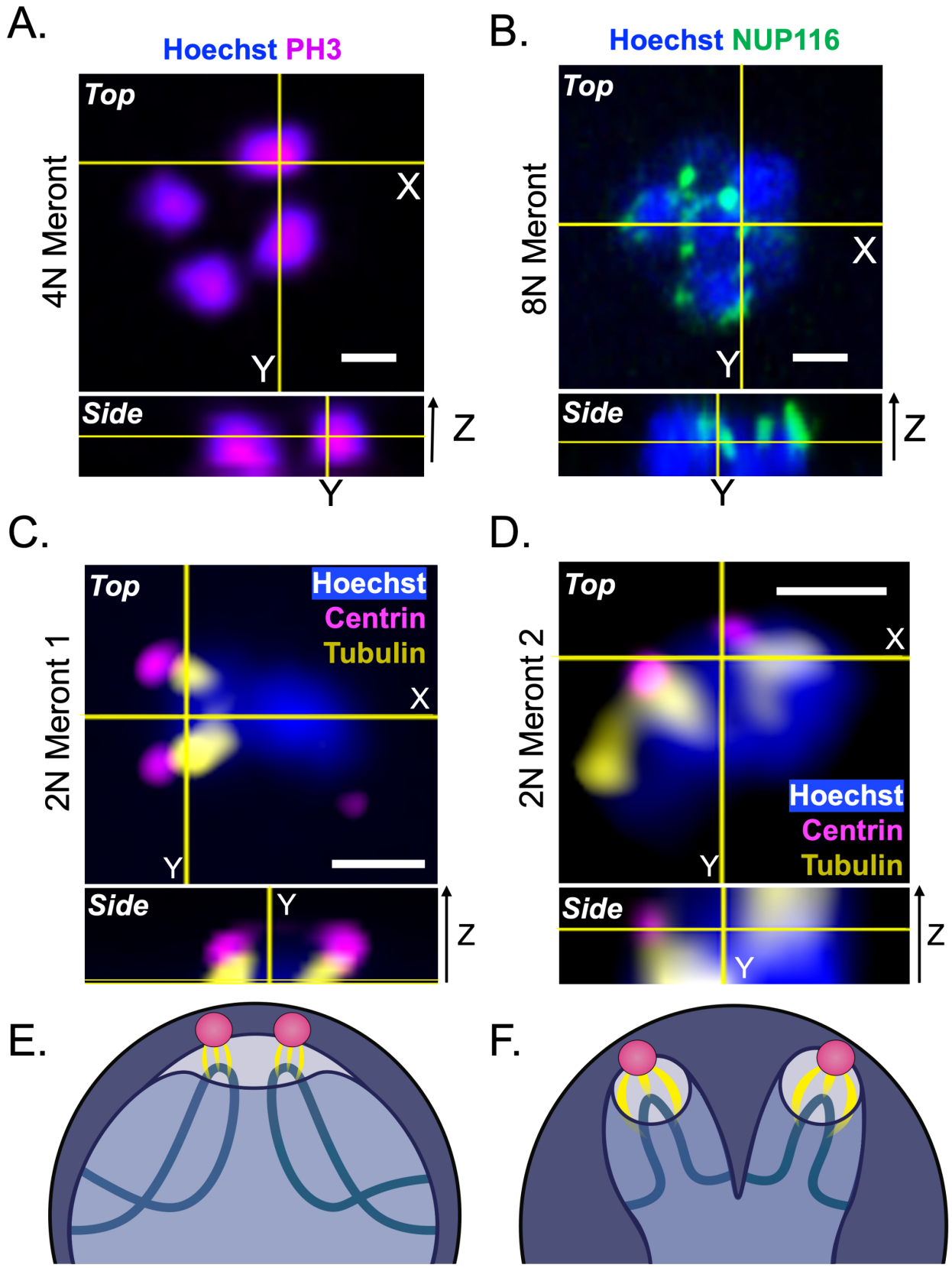
A.
Hoechst PH3
4N Meront
Top
X
Y
Side
Z
Y
B.
Hoechst NUP116
8N Meront
Top
X
Y
Side
Z
Y
C.
2N Meront 1
Top
Hoechst
Centrin
Tubulin
X
Y
Side
Y
Z
D.
2N Meront 2
Top
X
Hoechst
Centrin
Tubulin
Y
Side
Y
Z
E.
F.

630

631 **Figure 4: Mitotically active DNA, microtubules, and the nuclear pore proteins as visualized**
632 **by antibody staining in *C. parvum*.** (A) HCT-8 cells were infected with wild type parasites,
633 fixed at 18 hpi, and stained with rabbit anti-phosphorylated Histone H3 (PH3) followed by an
634 Alexa Fluor 568 goat anti-rabbit IgG antibody. DNA was stained with Hoechst and a mid-stage
635 meront with 4 nuclei is shown. (B) Parasites were prepared identically to panel A, but were
636 stained with an antibody that recognizes a subunit of the nuclear pore in *Plasmodium falciparum*
637 (NUP116) followed by an Alexa Fluor 568 goat anti-rabbit IgG antibody and Hoechst. A late-
638 stage meronts with 8 nuclei is shown. (C, D) HCT-8 cells were infected with wild type parasites,
639 fixed at 6.5 hpi to capture early meronts (2 nuclei), and stained with rabbit anti-centrin-1, mouse
640 anti-tubulin, and VVL-Biotin, followed by the secondary antibodies Alexa Fluor 488 goat anti-
641 mouse IgG, Alexa Fluor 568 goat anti-rabbit IgG, Alexa Fluor 647 Streptavidin, and Hoechst.
642 The nucleus in the first meront (C) is likely an example of early mitosis, whereas the second
643 meront (D) is likely an example of a later phase of the mitotic process. Images were acquired as
644 Z-stacks using LSCM-A and are presented with orthogonal views. Scale bars, 1 µm. (E) A
645 cartoon representation of the mitotic structures visualized in (C). The pink circles represent
646 centrin, which is localized to the intact nuclear envelope. Yellow microtubules originate from the
647 centriole-equivalent structures and attach to the uncondensed chromosomes visualized by
648 Hoechst. (F) A cartoon representation of the mitotic structures visualized in (D). Later in mitosis,
649 the microtubules (yellow) become more prominent and the centriole-equivalent structures (pink)
650 move away from one another, indicating active segregation and preparation for cytokinesis.
651

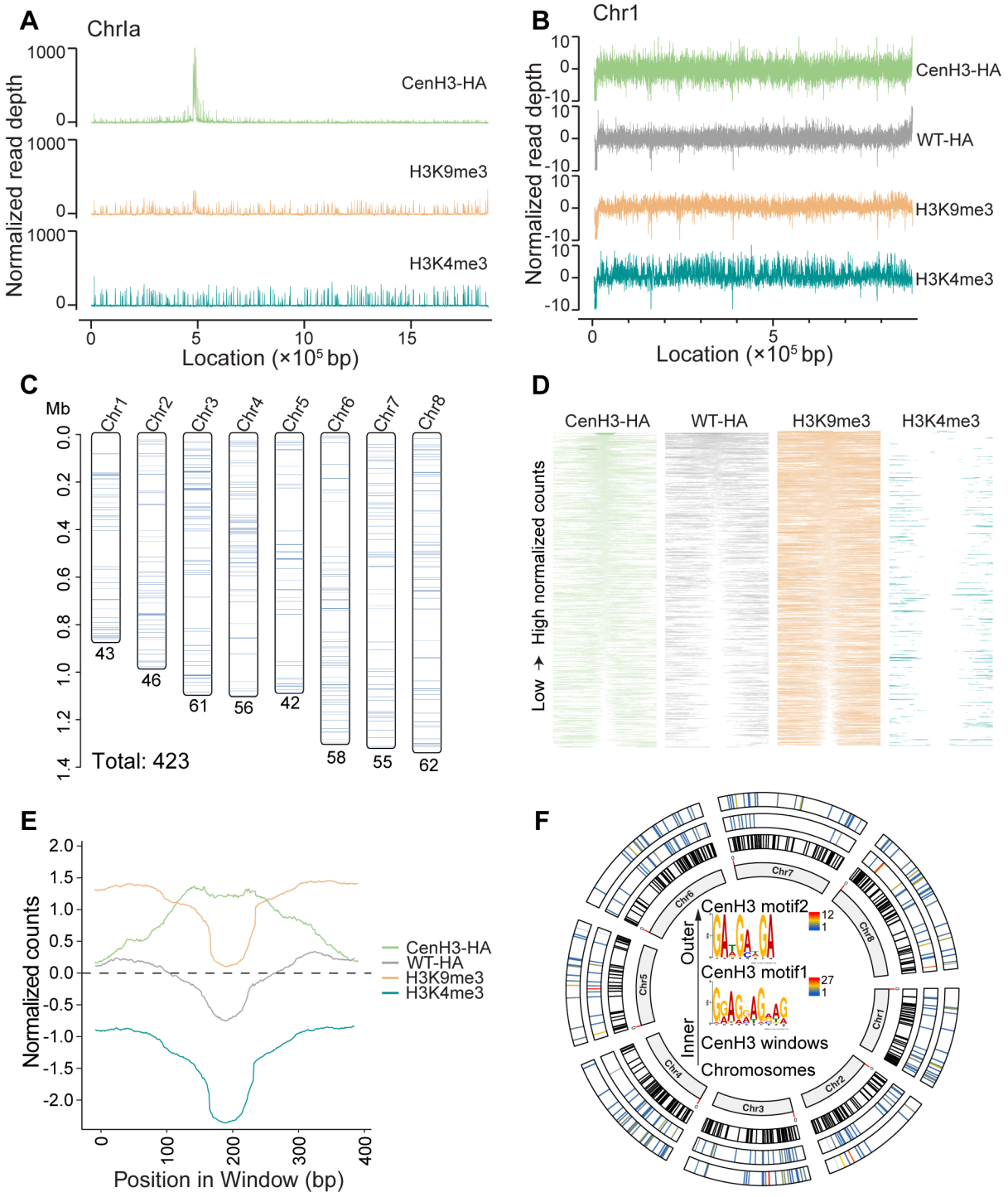

652

653 **Figure 5. Genome-wide distribution of CENH3 in *Toxoplasma gondii* and *Cryptosporidium***

654 ***parvum***. (A) Genome browser view of *T. gondii* chromosome Ia showing CUT&RUN signals for

655 CENH3-HA (HA antibody), H3K9me3, and H3K4me3. CENH3 signal enrichment positively

656 correlates with H3K9me3 and inversely with H3K4me3. Peaks of CENH3 enrichment are
657 indicated (red arrows). (B) Genome browser view of *C. parvum* chromosome I, showing
658 CUT&RUN signals for CENH3-HA *C. parvum* captured with HA antibody and wild type *C.*
659 *parvum* captured with HA antibody (referred to as WT-HA), H3K9me3, and H3K4me3
660 (captured with antibodies). (C) Chromosomal distribution of the 423 CENH3-enriched windows
661 in *C. parvum* chromosomes (Chr#). Numbers below each chromosome indicate the number of
662 windows. (D) Heatmaps of CUT&RUN signals for the groups shown in (B) within a 400 bp
663 window around all 423 centromeric windows. Each row represents an individual centromeric
664 site, ranked by signal intensity. (E) Average signal profiles for CENH3-HA (green), WT-HA
665 (gray), H3K9me3 (orange), and H3K4me3 (teal) across the 400 bp window around CENH3 sites.
666 (F) Circos plot of CENH3-associated motifs. From inner to outer rings: chromosomes,
667 centromeric window locations (black), motif 1 density, and motif 2 density. Representative
668 sequence logos for motif 1 and motif 2 are shown.
669
670
671
672
673
674
675
676
677
678

679

680 **Table 1:** The results of BLASTP analyses using the *C. parvum* centromeric histone H3-like protein (*cgd4_2030*), histone H3-like

681 proteins (*cgd3_2540* and *cgd4_3220).*

682

Top hits in Apicomplexa*	**E value**	**Top hits in all Eukaryotes#**	**E value**	**Top hits in *Saccharomyces cerevisiae***	**E value**	**Top hits in *Homo sapiens***	**E value**
histone H3-like centromeric protein CSE4 [*C. cionae*]	5e-46	centromeric DNA-binding histone H3-like protein cse4 [*N. ribis*]	3e-39	Chain A, Cse4	2e-30	Chain A, Histone H3.1, Histone H3-like centromeric protein A, Histone H3.1	5e-39
histone H3 [*C. cionae*]	2e-86	histone H3-like [*P. hypophthalmus*]	3e-86	histone H3	4e-81	histone H3.2	1e-88
histone H3 [*C. cionae*]	2e-90	histone H3-like [*P. hypophthalmus*]	2e-87	histone H3	2e-81	histone H3.2	1e-89

683 * *C. parvum* proteins were compared against all organisms in the Apicomplexa phylum (except for *Cryptosporidium* spp.),

684 # *C. parvum* proteins were compared against all organisms (except for Apicomplexa)

685 **Table 2:** The identity and similarity results from multiple global sequence alignments between H3.1, H3.2, and CENH3 proteins using

686 a BLOSUM62 scoring matrix.

***Cp* H3.1 and *Cp* H3.2**	***Cp* CENH3 and *Cp* H3.1**	***Cp* CENH3 and *Cp* H3.2**
	Identity: 46.31% Similarity: 65.10% Gaps: 14.09%	
Identity: 97.78% Similarity: 99.26% Gaps: 0.00%		Identity: 46.31% Similarity: 64.43% Gaps: 14.09%

687

688
689 **REFERENCES:**
690

691 1. Tyzzer E. An extracellular coccidium, Cryptosporidium muris (gen. et sp. nov.) of the
692 gastric glands of the common mouse. J Med Res. 1910;23:487-509. PubMed Central
693 PMCID: PMCPMC2098948.
694 2. Greenberg PD, Koch J, Cello JP. Diagnosis of Cryptosporidium parvum in patients with
695 severe diarrhea and AIDS. Dig Dis Sci. 1996;41(11):2286-90.
696 3. Striepen B. Parasitic infections: Time to tackle cryptosporidiosis. Nature.
697 2013;503(7475):189-91. PubMed Central PMCID: PMC24236315
698 4. Tzipori S, Widmer G. A hundred-year retrospective on cryptosporidiosis. Trends Parasitol.
699 2008;24(4):184-9. Epub 20080307. doi: 10.1016/j.pt.2008.01.002. PubMed PMID:
700 18329342; PubMed Central PMCID: PMCPMC2716703.
701 5. Sow SO, Muhsen K, Nasrin D, Blackwelder WC, Wu Y, Farag TH, et al. The Burden of
702 Cryptosporidium Diarrheal Disease among Children < 24 Months of Age in
703 Moderate/High Mortality Regions of Sub-Saharan Africa and South Asia, Utilizing
704 Data from the Global Enteric Multicenter Study (GEMS). PLoS Negl Trop Dis.
705 2016;10(5):e0004729. Epub 2016/05/25. doi: 10.1371/journal.pntd.0004729. PubMed
706 PMID: 27219054; PubMed Central PMCID: PMCPMC4878811.
707 6. Kotloff KL, Nataro JP, Blackwelder WC, Nasrin D, Farag TH, Panchalingam S, et al.
708 Burden and aetiology of diarrhoeal disease in infants and young children in developing
709 countries (the Global Enteric Multicenter Study, GEMS): a prospective, case-control
710 study. Lancet. 2013;382(9888):209-22.
711 7. Wanyiri JW, Kanyi H, Maina S, Wang DE, Steen A, Ngugi P, et al. Cryptosporidiosis in
712 HIV/AIDS patients in Kenya: clinical features, epidemiology, molecular
713 characterization and antibody responses. Am J Trop Med Hyg. 2014;91(2):319-28.
714 Epub 2014/05/29. doi: 10.4269/ajtmh.13-0254. PubMed PMID: 24865675; PubMed
715 Central PMCID: PMCPMC4125256.
716 8. Funkhouser-Jones LJ, Ravindran S, Sibley LD. Defining Stage-Specific Activity of Potent
717 New Inhibitors of Cryptosporidium parvum Growth In Vitro. mBio. 2020;11(2). Epub
718 2020/03/05. doi: 10.1128/mBio.00052-20. PubMed PMID: 32127445; PubMed
719 Central PMCID: PMCPMC7064746.
720 9. English ED, Guerin A, Tandel J, Striepen B. Live imaging of the Cryptosporidium parvum
721 life cycle reveals direct development of male and female gametes from type I meronts.
722 PLoS Biol. 2022;20(4):e3001604. Epub 2022/04/19. doi:
723 10.1371/journal.pbio.3001604. PubMed PMID: 35436284; PubMed Central PMCID:
724 PMCPMC9015140.
725 10. Beyer TV, Svezhova NV, Sidorenko NV, Khokhlov SE. Cryptosporidium parvum
726 (Coccidia, Apicomplexa): Some new ultrastructural observations on its endogenous
727 development. European Journal of Protistology. 2000;36(2):151-9. doi:
728 10.1016/s0932-4739(00)80034-6.
729 11. Pohlenz J, Bemrick WJ, Moon HW, Cheville NF. Bovine cryptosporidiosis: a transmission
730 and scanning electron microscopic study of some stages in the life cycle and of the
731 host-parasite relationship. Vet Pathol. 1978;15(3):417-27. Epub 1978/05/01. doi:
732 10.1177/030098587801500318. PubMed PMID: 98896.

733 12. Tzipori S, McCartney E, Lawson GH, Rowland AC, Campbell I. Experimental infection of
734 piglets with cryptosporidium. Res Vet Sci. 1981;31(3):358-68. Epub 1981/11/01.
735 PubMed PMID: 7342229.
736 13. Current WL, Reese NC. A comparison of endogenous development of three isolates of
737 Cryptosporidium in suckling mice. J Protozool. 1986;33(1):98-108. Epub 1986/02/01.
738 PubMed PMID: 3959014.
739 14. Keithly JS, Langreth SG, Buttle KF, Mannella CA. Electron tomographic and
740 ultrastructural analysis of the Cryptosporidium parvum relict mitochondrion, its
741 associated membranes, and organelles. J Eukaryot Microbiol. 2005;52(2):132-40.
742 Epub 2005/04/09. doi: 10.1111/j.1550-7408.2005.04-3317.x. PubMed PMID:
743 15817118.
744 15. Wilke G. Development of an in vitro Culture System for Cryptosporidium parvum. Theses
745 and Dissertations: Washington University in St. Louis; 2020.
746 16. White MW, Suvorova ES. Apicomplexa Cell Cycles: Something Old, Borrowed, Lost, and
747 New. Trends Parasitol. 2018;34(9):759-71. Epub 20180802. doi:
748 10.1016/j.pt.2018.07.006. PubMed PMID: 30078701; PubMed Central PMCID:
749 PMCPMC6157590.
750 17. Striepen B, Jordan CN, Reiff S, van Dooren GG. Building the perfect parasite: cell division
751 in apicomplexa. PLoS Pathog. 2007;3(6):e78. doi: 10.1371/journal.ppat.0030078.
752 PubMed PMID: 17604449; PubMed Central PMCID: PMCPMC1904476.
753 18. Gissot M, Walker R, Delhaye S, Huot L, Hot D, Tomavo S. Toxoplasma gondii
754 chromodomain protein 1 binds to heterochromatin and colocalises with centromeres
755 and telomeres at the nuclear periphery. PLoS One. 2012;7(3):e32671. Epub 20120309.
756 doi: 10.1371/journal.pone.0032671. PubMed PMID: 22427862; PubMed Central
757 PMCID: PMCPMC3302879.
758 19. Duraisingh MT, Voss TS, Marty AJ, Duffy MF, Good RT, Thompson JK, et al.
759 Heterochromatin silencing and locus repositioning linked to regulation of virulence
760 genes in Plasmodium falciparum. Cell. 2005;121(1):13-24. doi:
761 10.1016/j.cell.2005.01.036. PubMed PMID: 15820675.
762 20. del Cacho E, Pages M, Gallego M, Barbero JL, Monteagudo L, Sanchez-Acedo C. Meiotic
763 chromosome pairing and bouquet formation during Eimeria tenella sporulation. Int J
764 Parasitol. 2010;40(4):453-62. Epub 20091029. doi: 10.1016/j.ijpara.2009.09.008.
765 PubMed PMID: 19837073.
766 21. Dey G, Culley S, Curran S, Schmidt U, Henriques R, Kukulski W, et al. Closed mitosis
767 requires local disassembly of the nuclear envelope. Nature. 2020;585(7823):119-23.
768 Epub 20200826. doi: 10.1038/s41586-020-2648-3. PubMed PMID: 32848252;
769 PubMed Central PMCID: PMCPMC7610560.
770 22. Matthews H, Duffy CW, Merrick CJ. Checks and balances? DNA replication and the cell
771 cycle in Plasmodium. Parasit Vectors. 2018;11(1):216. Epub 20180327. doi:
772 10.1186/s13071-018-2800-1. PubMed PMID: 29587837; PubMed Central PMCID:
773 PMCPMC5872521.
774 23. Rout MP, Obado SO, Schenkman S, Field MC. Specialising the parasite nucleus: Pores,
775 lamins, chromatin, and diversity. PLoS Pathog. 2017;13(3):e1006170. Epub
776 20170302. doi: 10.1371/journal.ppat.1006170. PubMed PMID: 28253370; PubMed
777 Central PMCID: PMCPMC5333908.

24. Suvorova ES, Francia M, Striepen B, White MW. A novel bipartite centrosome coordinates the apicomplexan cell cycle. PLoS Biol. 2015;13(3):e1002093. Epub 20150303. doi: 10.1371/journal.pbio.1002093. PubMed PMID: 25734885; PubMed Central PMCID: PMCPMC4348508.
25. Chen CT, Kelly M, Leon J, Nwagbara B, Ebbert P, Ferguson DJ, et al. Compartmentalized Toxoplasma EB1 bundles spindle microtubules to secure accurate chromosome segregation. Mol Biol Cell. 2015;26(25):4562-76. Epub 20151014. doi: 10.1091/mbc.E15-06-0437. PubMed PMID: 26466679; PubMed Central PMCID: PMCPMC4678015.
26. Hoeijmakers WA, Flueck C, Francoijs KJ, Smits AH, Wetzel J, Volz JC, et al. Plasmodium falciparum centromeres display a unique epigenetic makeup and cluster prior to and during schizogony. Cell Microbiol. 2012;14(9):1391-401. Epub 20120515. doi: 10.1111/j.1462-5822.2012.01803.x. PubMed PMID: 22507744.
27. Brooks CF, Francia ME, Gissot M, Croken MM, Kim K, Striepen B. Toxoplasma gondii sequesters centromeres to a specific nuclear region throughout the cell cycle. Proc Natl Acad Sci U S A. 2011;108(9):3767-72. Epub 20110214. doi: 10.1073/pnas.1006741108. PubMed PMID: 21321216; PubMed Central PMCID: PMCPMC3048097.
28. Arnot DE, Ronander E, Bengtsson DC. The progression of the intra-erythrocytic cell cycle of Plasmodium falciparum and the role of the centriolar plaques in asynchronous mitotic division during schizogony. Int J Parasitol. 2011;41(1):71-80. Epub 20100917. doi: 10.1016/j.ijpara.2010.07.012. PubMed PMID: 20816844.
29. Iwanaga S, Khan SM, Kaneko I, Christodoulou Z, Newbold C, Yuda M, et al. Functional identification of the Plasmodium centromere and generation of a Plasmodium artificial chromosome. Cell Host Microbe. 2010;7(3):245-55. doi: 10.1016/j.chom.2010.02.010. PubMed PMID: 20227667; PubMed Central PMCID: PMCPMC2996609.
30. Absalon S. A dynamic barrier: remodeling of the nuclear envelope during closed mitosis in malaria parasites. mSphere. 2025;10(7):e0099924. Epub 20250609. doi: 10.1128/msphere.00999-24. PubMed PMID: 40488521; PubMed Central PMCID: PMCPMC12306155.
31. Weiner A, Dahan-Pasternak N, Shimoni E, Shinder V, von Huth P, Elbaum M, et al. 3D nuclear architecture reveals coupled cell cycle dynamics of chromatin and nuclear pores in the malaria parasite Plasmodium falciparum. Cell Microbiol. 2011;13(7):967-77. Epub 20110428. doi: 10.1111/j.1462-5822.2011.01592.x. PubMed PMID: 21501361.
32. Francia ME, Striepen B. Cell division in apicomplexan parasites. Nat Rev Microbiol. 2014;12(2):125-36. Epub 20140102. doi: 10.1038/nrmicro3184. PubMed PMID: 24384598.
33. Kursel LE, Malik HS. Centromeres. Curr Biol. 2016;26(12):R487-R90. doi: 10.1016/j.cub.2016.05.031. PubMed PMID: 27326706.
34. Hegemann JH, Fleig UN. The centromere of budding yeast. Bioessays. 1993;15(7):451-60. doi: 10.1002/bies.950150704. PubMed PMID: 8379948.
35. Kelly JM, McRobert L, Baker DA. Evidence on the chromosomal location of centromeric DNA in Plasmodium falciparum from etoposide-mediated topoisomerase-II cleavage. Proc Natl Acad Sci U S A. 2006;103(17):6706-11. Epub 20060414. doi:

823 10.1073/pnas.0510363103. PubMed PMID: 16617116; PubMed Central PMCID:
824 PMCPMC1458945.
825 36. Viera A, Page J, Rufas JS. Inverted meiosis: the true bugs as a model to study. Genome
826 Dyn. 2009;5:137-56. doi: 10.1159/000166639. PubMed PMID: 18948713.
827 37. Mandrioli M, Manicardi GC. Holocentric chromosomes. PLoS Genet.
828 2020;16(7):e1008918. Epub 20200730. doi: 10.1371/journal.pgen.1008918. PubMed
829 PMID: 32730246; PubMed Central PMCID: PMCPMC7392213.
830 38. Marques A, Drinnenberg IA. Same but different: Centromere regulations in holocentric
831 insects and plants. Curr Opin Cell Biol. 2025;93:102484. Epub 20250220. doi:
832 10.1016/j.ceb.2025.102484. PubMed PMID: 39983583.
833 39. Bensasson D. Evidence for a high mutation rate at rapidly evolving yeast centromeres.
834 BMC Evol Biol. 2011;11:211. Epub 20110718. doi: 10.1186/1471-2148-11-211.
835 PubMed PMID: 21767380; PubMed Central PMCID: PMCPMC3155921.
836 40. Csink AK, Henikoff S. Something from nothing: the evolution and utility of satellite
837 repeats. Trends Genet. 1998;14(5):200-4. doi: 10.1016/s0168-9525(98)01444-9.
838 PubMed PMID: 9613205.
839 41. Talbert PB, Henikoff S. Centromeres drive and take a break. Chromosome Res.
840 2025;33(1):17. Epub 20250804. doi: 10.1007/s10577-025-09777-z. PubMed PMID:
841 40759764; PubMed Central PMCID: PMCPMC12321929.
842 42. Henikoff S, Ahmad K, Malik HS. The centromere paradox: stable inheritance with rapidly
843 evolving DNA. Science. 2001;293(5532):1098-102. doi: 10.1126/science.1062939.
844 PubMed PMID: 11498581.
845 43. Talbert PB, Henikoff S. What makes a centromere? Exp Cell Res. 2020;389(2):111895.
846 Epub 20200206. doi: 10.1016/j.yexcr.2020.111895. PubMed PMID: 32035948.
847 44. Skene PJ, Henikoff S. An efficient targeted nuclease strategy for high-resolution mapping
848 of DNA binding sites. Elife. 2017;6. Epub 20170116. doi: 10.7554/eLife.21856.
849 PubMed PMID: 28079019; PubMed Central PMCID: PMCPMC5310842.
850 45. Herrera-Solorio AM, Vembar SS, MacPherson CR, Lozano-Amado D, Meza GR,
851 Xoconostle-Cazares B, et al. Clipped histone H3 is integrated into nucleosomes of
852 DNA replication genes in the human malaria parasite Plasmodium falciparum. EMBO
853 Rep. 2019;20(4). Epub 20190304. doi: 10.15252/embr.201846331. PubMed PMID:
854 30833341; PubMed Central PMCID: PMCPMC6446197.
855 46. Verma G, Surolia N. Plasmodium falciparum CENH3 is able to functionally complement
856 Cse4p and its, C-terminus is essential for centromere function. Mol Biochem Parasitol.
857 2013;192(1-2):21-9. Epub 20131206. doi: 10.1016/j.molbiopara.2013.11.002. PubMed
858 PMID: 24316361.
859 47. Naumov A, Kratzer S, Ting LM, Kim K, Suvorova ES, White MW. The Toxoplasma
860 Centrocone Houses Cell Cycle Regulatory Factors. mBio. 2017;8(4). Epub 20170822.
861 doi: 10.1128/mBio.00579-17. PubMed PMID: 28830940; PubMed Central PMCID:
862 PMCPMC5565962.
863 48. Mahajan B, Selvapandiyan A, Gerald NJ, Majam V, Zheng H, Wickramarachchi T, et al.
864 Centrins, cell cycle regulation proteins in human malaria parasite Plasmodium
865 falciparum. J Biol Chem. 2008;283(46):31871-83. Epub 20080808. doi:
866 10.1074/jbc.M800028200. PubMed PMID: 18693242.
867 49. Liu C, Wang L, Lancto CA, Abrahamsen MS. Characterization of a Cryptosporidium
868 parvum protein that binds single-stranded G-strand telomeric DNA. Mol Biochem

869 Parasitol. 2009;165(2):132-41. Epub 20090204. doi:
870 10.1016/j.molbiopara.2009.01.013. PubMed PMID: 19428660.
871 50. Ay F, Bunnik EM, Varoquaux N, Bol SM, Prudhomme J, Vert JP, et al. Three-dimensional
872 modeling of the P. falciparum genome during the erythrocytic cycle reveals a strong
873 connection between genome architecture and gene expression. Genome Res.
874 2014;24(6):974-88. Epub 20140326. doi: 10.1101/gr.169417.113. PubMed PMID:
875 24671853; PubMed Central PMCID: PMCPMC4032861.
876 51. Bunnik EM, Cook KB, Varoquaux N, Batugedara G, Prudhomme J, Cort A, et al. Changes
877 in genome organization of parasite-specific gene families during the Plasmodium
878 transmission stages. Nat Commun. 2018;9(1):1910. Epub 20180515. doi:
879 10.1038/s41467-018-04295-5. PubMed PMID: 29765020; PubMed Central PMCID:
880 PMCPMC5954139.
881 52. Hollin T, Le Roch KG. From Genes to Transcripts, a Tightly Regulated Journey in
882 Plasmodium. Front Cell Infect Microbiol. 2020;10:618454. Epub 20201217. doi:
883 10.3389/fcimb.2020.618454. PubMed PMID: 33425787; PubMed Central PMCID:
884 PMCPMC7793691.
885 53. McIntosh JR. Mitosis. Cold Spring Harb Perspect Biol. 2016;8(9). Epub 20160901. doi:
886 10.1101/cshperspect.a023218. PubMed PMID: 27587616; PubMed Central PMCID:
887 PMCPMC5008068.
888 54. Perez-Cadahia B, Drobic B, Davie JR. H3 phosphorylation: dual role in mitosis and
889 interphase. Biochem Cell Biol. 2009;87(5):695-709. doi: 10.1139/O09-053. PubMed
890 PMID: 19898522.
891 55. Gerald N, Mahajan B, Kumar S. Mitosis in the human malaria parasite Plasmodium
892 falciparum. Eukaryot Cell. 2011;10(4):474-82. Epub 20110211. doi:
893 10.1128/EC.00314-10. PubMed PMID: 21317311; PubMed Central PMCID:
894 PMCPMC3127633.
895 56. Steiner FA, Henikoff S. Holocentromeres are dispersed point centromeres localized at
896 transcription factor hotspots. Elife. 2014;3:e02025. Epub 20140101. doi:
897 10.7554/eLife.02025. PubMed PMID: 24714495; PubMed Central PMCID:
898 PMCPMC3975580.
899 57. Xia J, Venkat A, Bainbridge RE, Reese ML, Le Roch KG, Ay F, et al. Third-generation
900 sequencing revises the molecular karyotype for Toxoplasma gondii and identifies
901 emerging copy number variants in sexual recombinants. Genome Res. 2021;31(5):834-
902 51. Epub 20210427. doi: 10.1101/gr.262816.120. PubMed PMID: 33906962; PubMed
903 Central PMCID: PMCPMC8092015.
904 58. Steiner FA, Henikoff S. Holocentromeres are dispersed point centromeres localized at
905 transcription factor hotspots. Elife. 2014;3. doi: ARTN e02025
906 10.7554/eLife.02025. PubMed PMID: WOS:000334351700005.
907 59. Blauwkamp J, Ambekar SV, Hussain T, Mair GR, Beck JR, Absalon S. Nuclear pore
908 complexes undergo Nup221 exchange during blood-stage asexual replication of
909 parasites. Msphere. 2024;9(12). doi: 10.1128/msphere.00750-24. PubMed PMID:
910 WOS:001352594000001.
911 60. Edwards-Smallbone J, Jensen AL, Roberts LE, Totanes FIG, Hart SR, Merrick CJ.
912 Plasmodium falciparum GBP2 Is a Telomere-Associated Protein That Binds to G-
913 Quadruplex DNA and RNA. Front Cell Infect Microbiol. 2022;12:782537. Epub

914 20220222. doi: 10.3389/fcimb.2022.782537. PubMed PMID: 35273922; PubMed
915 Central PMCID: PMCPMC8902816.
916 61. Zhao N, Gong P, Li Z, Cheng B, Li J, Yang Z, et al. Identification of a telomeric DNA-
917 binding protein in Eimeria tenella. Biochem Biophys Res Commun. 2014;451(4):599-
918 602. Epub 20140813. doi: 10.1016/j.bbrc.2014.08.030. PubMed PMID: 25128826.
919 62. Yang D, Xiao Z, Li K, Hou J, Zhang F, Qiao J, et al. Eukaryotic Centromere Remodeling:
920 Plasticity, Dynamics, and Holocentromere Formation. Plant Cell Environ.
921 2025;48(9):6691-703. Epub 20250527. doi: 10.1111/pce.15652. PubMed PMID:
922 40421727.
923 63. Ishii K, Ogiyama Y, Chikashige Y, Soejima S, Masuda F, Kakuma T, et al.
924 Heterochromatin integrity affects chromosome reorganization after centromere
925 dysfunction. Science. 2008;321(5892):1088-91. doi: 10.1126/science.1158699.
926 PubMed PMID: 18719285.
927 64. Ketel C, Wang HS, McClellan M, Bouchonville K, Selmecki A, Lahav T, et al.
928 Neocentromeres form efficiently at multiple possible loci in Candida albicans. PLoS
929 Genet. 2009;5(3):e1000400. Epub 20090306. doi: 10.1371/journal.pgen.1000400.
930 PubMed PMID: 19266018; PubMed Central PMCID: PMCPMC2642679.
931 65. Melters DP, Paliulis LV, Korf IF, Chan SW. Holocentric chromosomes: convergent
932 evolution, meiotic adaptations, and genomic analysis. Chromosome Res.
933 2012;20(5):579-93. doi: 10.1007/s10577-012-9292-1. PubMed PMID: 22766638.
934 66. Lucek K, Augustijnen H, Escudero M. A holocentric twist to chromosomal speciation?
935 Trends Ecol Evol. 2022;37(8):655-62. Epub 20220426. doi:
936 10.1016/j.tree.2022.04.002. PubMed PMID: 35484024.
937 67. Funkhouser-Jones LJ, Xu R, Wilke G, Fu Y, Schriefer LA, Makimaa H, et al. Microbiota-
938 produced indole metabolites disrupt mitochondrial function and inhibit
939 Cryptosporidium parvum growth. Cell Rep. 2023;42(7):112680. Epub 2023/06/29.
940 doi: 10.1016/j.celrep.2023.112680. PubMed PMID: 37384526.
941 68. Pardy RD, Wallbank BA, Striepen B, Hunter CA. Immunity to Cryptosporidium: insights
942 into principles of enteric responses to infection. Nat Rev Immunol. 2024;24(2):142-55.
943 Epub 20230911. doi: 10.1038/s41577-023-00932-3. PubMed PMID: 37697084.
944 69. Martinez-Perez E, Schvarzstein M, Barroso C, Lightfoot J, Dernburg AF, Villeneuve AM.
945 Crossovers trigger a remodeling of meiotic chromosome axis composition that is
946 linked to two-step loss of sister chromatid cohesion. Genes Dev. 2008;22(20):2886-
947 901. doi: 10.1101/gad.1694108. PubMed PMID: 18923085; PubMed Central PMCID:
948 PMCPMC2569886.
949 70. Kimball A, Funkhouser-Jones L, Huang W, Xu R, Witola WH, Sibley LD. Mendelian
950 segregation and high recombination rates facilitate genetic analyses in
951 Cryptosporidium parvum. PLoS Genet. 2024;20(6):e1011162. Epub 20240617. doi:
952 10.1371/journal.pgen.1011162. PubMed PMID: 38885280; PubMed Central PMCID:
953 PMCPMC11213348.
954 71. Wilke G, Ravindran S, Funkhouser-Jones L, Barks J, Wang Q, VanDussen KL, et al.
955 Monoclonal antibodies to intracellular stages of *Cryptosporidium parvum* define life
956 cycle progression in vitro. mSphere. 2018;3(3):e00124-18. Epub 2018/06/01. doi:
957 10.1128/mSphere.00124-18. PubMed PMID: 29848759; PubMed Central PMCID:
958 PMCPMC5976880.

72. Xu R, Beatty WL, Greigert V, Witola WH, Sibley LD. Multiple pathways for glucose phosphate transport and utilization support growth of Cryptosporidium parvum. Nat Commun. 2024;15(1):380. Epub 20240109. doi: 10.1038/s41467-024-44696-3. PubMed PMID: 38191884; PubMed Central PMCID: PMCPMC10774378.
73. Wilke G, Funkhouser-Jones L, Wang Y, Ravindran S, Wang Q, Beatty WL, et al. Forward genetics in *Cryptosporidium* enabled by complete in vitro development in stem cell-derived intestinal epithlium. Cell Host Microbe. 2019;doi.org/10.2139/ssrn.3331307.
74. Xu R, Beatty WL, Greigert V, Witola WH, Sibley LD. Multiple pathways for glucose phosphate transport and utilization support growth of Cryptosporidium parvum. bioRxiv. 2023. Epub 2023/07/10. doi: 10.1101/2023.06.27.546703. PubMed PMID: 37425855; PubMed Central PMCID: PMCPMC10327089.
75. Akey ME, Xu R, Ravindran S, Funkhouser-Jones L, Sibley LD. Apical Secretory Glycoprotein Complex Contributes to Cell Attachment and Entry by Cryptosporidium parvum. mBio. 2023;14(1):e0306422. Epub 2023/02/02. doi: 10.1128/mbio.03064-22. PubMed PMID: 36722968; PubMed Central PMCID: PMCPMC9973360.
76. Xu R, Feng Y, Xiao L, Sibley LD. Insulinase-like Protease 1 Contributes to Macrogamont Formation in Cryptosporidium parvum. mBio. 2021;12(2). Epub 2021/03/11. doi: 10.1128/mBio.03405-20. PubMed PMID: 33688009; PubMed Central PMCID: PMCPMC8092296.
77. Kuhlenschmidt TB, Rutaganira FU, Long S, Tang K, Shokat KM, Kuhlenschmidt MS, et al. Inhibition of Calcium-Dependent Protein Kinase 1 (CDPK1) In Vitro by Pyrazolopyrimidine Derivatives Does Not Correlate with Sensitivity of Cryptosporidium parvum Growth in Cell Culture. Antimicrob Agents Chemother. 2015;60(1):570-9.
78. Current WL. Techniques and laboratory maintenance of *Cryptosporidium*. In: Dubey JP, Speer CA, Fayer R, editors. Cryptosporidiosis of Man and Animals. Boca Raton, FL: CRC Press; 1990. p. 44-77.
79. Mehta S, Sibley LD. Actin depolymerizing factor controls actin turnover and gliding motility in Toxoplasma gondii. Mol Biol Cell. 2011;22(8):1290-9. Epub 20110223. doi: 10.1091/mbc.E10-12-0939. PubMed PMID: 21346192; PubMed Central PMCID: PMCPMC3078074.
80. Behnke MS, Radke JB, Smith AT, Sullivan WJ, Jr., White MW. The transcription of bradyzoite genes in Toxoplasma gondii is controlled by autonomous promoter elements. Mol Microbiol. 2008;68(6):1502-18. Epub 20080421. doi: 10.1111/j.1365-2958.2008.06249.x. PubMed PMID: 18433450; PubMed Central PMCID: PMCPMC2440561.
81. Waldman BS, Schwarz D, Wadsworth MH, 2nd, Saeij JP, Shalek AK, Lourido S. Identification of a Master Regulator of Differentiation in Toxoplasma. Cell. 2020;180(2):359-72 e16. Epub 20200116. doi: 10.1016/j.cell.2019.12.013. PubMed PMID: 31955846; PubMed Central PMCID: PMCPMC6978799.
82. Huang W, Tang K, Chen C, Arrowood MJ, Chen M, Guo Y, et al. Sequence introgression from exogenous lineages underlies genomic and biological differences among Cryptosporidium parvum IOWA lines. Water Res. 2024;254:121333. Epub 2024/02/26. doi: 10.1016/j.watres.2024.121333. PubMed PMID: 38402753; PubMed Central PMCID: PMCPMC10994760.